ALGOL

SPEKTROHELIOGRAPHIE

LUTETIUM AUF DER SONNE

ALGOL

SPECTROHELIOGRAPHY

LUTETIUM ON SUN

Impressum

Die Fachgruppe Spektroskopie im Internet: spektroskopie.fg-vds.de

Die Vereinigung der Sternfreunde e.V. im Internet: www.vds-astro.de

Kontaktadresse (Redaktion, Bestellung gedruckter Ausgaben, Einsendung von Manuskripten)

Dr. Thomas Hunger
Weinbergstraße 12
D-01129 Dresden
thunger03@web.de

Hinweise für Autoren:
Nur durch Ihre Artikel wird Spektrum gefüllt. Die Redaktion behält sich vor, in Rücksprache mit den Autoren Beiträge zu kürzen, anzupassen oder zu ändern. Für die Inhalte der Artikel ist aber allein der Autor verantwortlich. Mit der Einreichung eines Beitrages erklärt der/die Autor(en) die Bereitschaft zur Publikation auch im Journal für Astronomie der VdS e.V.
Reichen sie Ihren Beitrag bitte elektronisch unter Berücksichtigung folgender Regeln ein:
Form des Textes: Senden sie vorzugsweise als unformatierten ASCII-Text. Tabellen mit Tabulatoren getrennt. Ein zusätzliches PDF des formatierten Gesamttextes ist anzuraten.
Aufbau der Artikel: Die Artikel benötigen einen Titel, eine vollständige Adressangabe des Autors / der Autoren, eine Kurzzusammenfassung, den klar gegliederten Artikel mit Einleitung und Zusammenfassung sowie eine vollständige Literaturangabe.
Abbildungen: Bitte getrennt vom Text senden. Empfehlenswert sind hochauflösende JPG, PNG und TIFF.
Hints for authors:
Your article will be edited to fit the style of Spektrum. The editor is responsible for editing the article in close collaboration with the author. The author is in charge of the content in all cases, however. The author(s) give(s) the permission for a further publication of the contribution in the journal of the VdS e.V. (Journal für Astronomie) right with its transfer to the editor of Spektrum. Please send your contribution via electronic mail considering the following rules:
Text: Prepare it as unformatted text (preferably ASCII). Tables: columns separated by tabs. A PDF printout of the whole document is highly recommended.
Article structure: Each article should include a title, an address line of the author(s), an abstract, a clear text body with introduction and conclusion and complete references.
Figures: Please send them separate from text. High resolution JPG, PNG or TIFF files are recommended.

Umschlagfoto: Spektroheliogramme bei verschiedenen Wellenlängen. Mehr dazu im Beitrag von Peter Zetner.

Inhaltsverzeichnis / Content

Editorial

Liebe Leser des Spektrums,
liebe Fachgruppenmitglieder,

die ASpekt 17 in St. Niklausen nahe Luzern ist schon wieder Geschichte. Eine erfolgreiche Tagung mit unseren Schweizer Freunden in einem wunderschönen Ambiente wird allen Beteiligten in Erinnerung beiben. Herzlichen Dank nochmals an das Orga-Team Patricia Otero und Rainer Borchmann.

Während der ASpekt wurde das Sprecherteam neu gewählt: Rainer Borchmann wurde für weitere vier Jahre als Sprecher wiedergewählt, Ulrich Waldschläger und Thomas Hunger werden als Vertreter beisitzen.

Der Versand der nun vorliegenden Ausgabe von Spektrum hat sich bis in den Juni verzögert. Die Fertigstellung hat deutlich mehr Zeit in Anspruch genommen, als ursprünglich geplant. Allerdings hat sich das Warten gelohnt, da damit der Artikel von Peter Zetner aufgenommen werden konnte – diesmal als Zweitveröffentlichung aus SONNE. Danke an das SONNE Team für diese Möglichkeit.

Mit sternfreundlichen Grüßen,
Ihr Thomas Hunger

Dear readers of Spektrum,
Dear members of the section,

The ASpekt 17 in St. Niklausen near Lucerne is already history. A successful conference with our Swiss friends in a beautiful ambience will be remembered by everyone involved. Thanks again to the organization team Patricia Otero and Rainer Borchmann.

During the ASpekt, the election of the speaker and its substitute speakers took place: Rainer Borchmann was re-elected for another four years, Ulrich Waldschläger and Thomas Hunger were appointed as substitutes.

The distribution of the now available issue of Spektrum has been delayed until June. Completion took significantly longer than originally planned. However, the wait was worth it, as the article by Peter Zetner could be included – this time as a second publication from SONNE. Thanks to the team of SONNE for this opportunity.

Clear skies.
Yours Thomas Hunger

Spectroscopic study of the mass transfer in the β Per binary system

Bernd Bitnar[1], Ulrich Waldschläger
[1] Heinrich-Heine-Str. 2E, 01728 Bannewitz, Germany, Email: bernd.bitnar@gmx.de

Abstract
The Hα profile of the eclipsing binary system Algol (β Per) shows a specific emission structure, which originates from a hot spot in a gas flow from the K2 secondary to the B8 primary star. The Hα emission was measured during an 18-month observation period to study their temporal stability. No significant variability has been observed. Further, an analysis of the radial velocity of the emission structure as a function of the orbital phase shows, that the origin of the emission is in the outer part of the system relatively close to the K2 secondary star.

Zusammenfassung
Das Profil der Hα Linie des Bedeckungsveränderlichen Algol (β Per) weist eine spezifische Emissions-struktur auf, die in einem Hot Spot innerhalb eines Gasstroms vom K2 Begleiter auf den B8 Hauptstern entsteht. Diese Emissionsstruktur wurde über einen Zeitraum von 18 Monaten verfolgt, um deren zeitli-che Stabilität zu untersuchen. Hinweise auf eine signifikante Veränderlichkeit wurden dabei nicht gefun-den. Weiterhin konnte durch eine Analyse der Radialgeschwindigkeit der Emissionsstruktur über deren Bahnumlauf gezeigt werden, dass die Emission im äußeren Bereich des Systems in der Nähe des K2 Begleitsterns entsteht.

1. Introduction

Algol (β Per) is the prototype of an eclipsing binary system, in which the primary component is a hot main sequence star and the secondary is a cool giant, which fills its Roche lobe. This means that gas is flowing from the secondary to the primary star, typically forming an accretion disc around the primary. A hot spot is formed where the gas flow is getting in contact to the accretion disc.

In the case of β Per the inclination of the orbit is close to 90°, so that for a terrestrial observer a periodical occultation of the primary star due to the secondary occurs.

In an earlier publication [1] a conspicuous emission line embedded in the Hα absorption of the eclipsing binary system β Per was described. This emission was observed especially close to the phase angles 0.25 and 0.75 of the orbit. The phase 0.0 is defined as the occultation of the primary due to the secondary star.

In this work, the emission structure was investigated in more detail. Spectra were taken during an 18-month period to study their temporal stability. In addition, the radial velocity as a function of the phase angle of the orbital position was investigated to examine the origin of the emission.

2. Experimental setup

The spectra were recorded from two observatories in Bannewitz, Saxonia, and in Berlin. Bannewitz used a Lhires III spectrograph [1] together with either a C8 or a 16" RC telescope. The Lhires spectrograph was equipped with a 2400 l/mm grating and a 23 µm slit. The spectra were taken with a Σ 1603 CCD camera with 1.6 MPixel and 9x9 µm² pixel size. The spectral coverage with this setup for a typical Hα spectrum is the range from 6500 to 6650 Å with a resolution of around 15000. For guiding a Starlight Xpress Lodestar camera was used coupled to the guiding port of the Lhires. The typical exposure time for the spectra was 900 s. With that a typical SNR (signal-to-noise-ratio) of about 100 – 150 for the C8 and about 200 – 300 for the 16" RC telescope was achieved.

In Berlin, a 10" Meade LX200 together with a fiber coupled Czerny-Turner spectrograph was used. The slit width was 30 µm. The typical exposure time was 2400 – 3600 s.

For the extraction and calibration of the spectra the software vspec [2] was used. The removal of the telluric H2O lines (drying) and the fine calibration of the wavelength was carried out with SpectroTools [3].

The Hα line profiles were fitted by a pseudo Voigt profile, that is a sum of a Lorentz- and a Gauß-Function. Details of this fitting procedure are described in [1].

All spectra in this article are plotted as a function of the radial velocity of the Hα line after correction of the heliocentric velocity.

3. Hα line profiles for different orbital phase positions

β Per is a triple system. In this investigation only the inner components – A and B – have been studied. Table 1 lists some physical parameters of the A and B components of β Per from [4, 5].

Spectral type	B8V + K2IV
Mass [sun mass]	3.39 + 0.77
Radius [sun radius]	2.9 + 3.4
Temperature [K]	12550 + 4900
Radial velocity V [km/s]	4.0
Period [d]	2.8714
Inclination	97.69°
Eccentricity	0.0
KA [km/s]	44.1 ± 0.2
KB [km/s]	194.2 ± 1.2
Distance [Pc]	31 ± 3

Tab. 1: List of physical parameters of β Per [4, 5]. V is the radial velocity of the mass center of the triple system, KA and KB denote the radial velocity amplitudes of the A and the B component, resp.

In the following, typical spectra of the Hα line of β Per for specific orbital positions are shown. Figure 1 shows the Hα profile for phase 0.99 close to the optical occultation at phase 0.0. The measured spectrum is shown in red together with a pseudo Voigt fit (blue), which is able to represent the spectrum very well. It is assumed that only radiation from the B8 primary component contributes to the Hα absorption line. Signatures from the K2 secondary star as well as from the outer C component are not visible in the spectrum.

This Hα profile of phase 0.0 together with its pseudo Voigt fit function will be considered in the following to study deviations from the primary star absorption profile during the orbital trajectory of the binary.

Figure 2 shows the Hα profile at the orbital phase of 0.28.

By comparing the measured spectrum with a pseudo Voigt fit an emission line is clearly visible, which shows a radial velocity of

(94 ± 10) km/s. The radial velocity of the primary star, which is given by the minimum of the absorption line, is blue shifted.
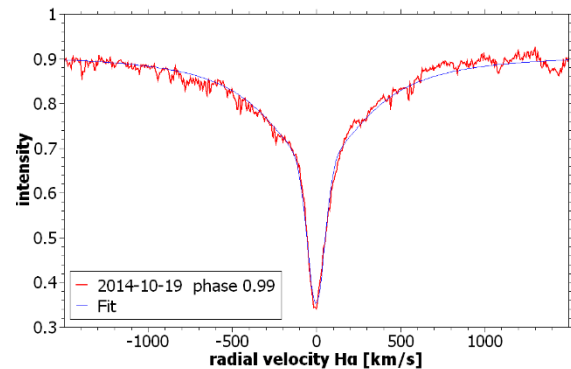
Fig. 1: Spectrum of the Hα line of β Per close to the optical minimum at phase 0.99 (red). A pseudo Voigt fit (blue) is shown for comparison.
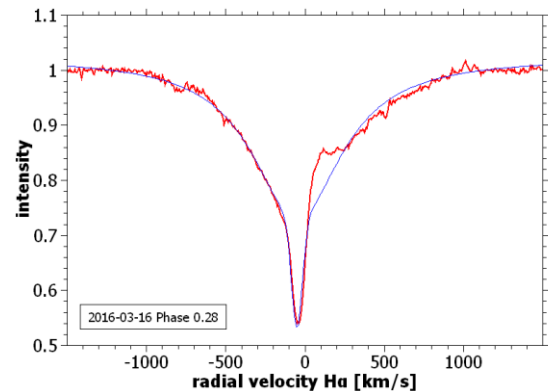
Fig. 2: Hα line of β Per at the orbital phase of 0.28. By comparing the observed spectrum (red) with a pseudo Voigt fit (blue) a red shifted emission line is clearly visible.
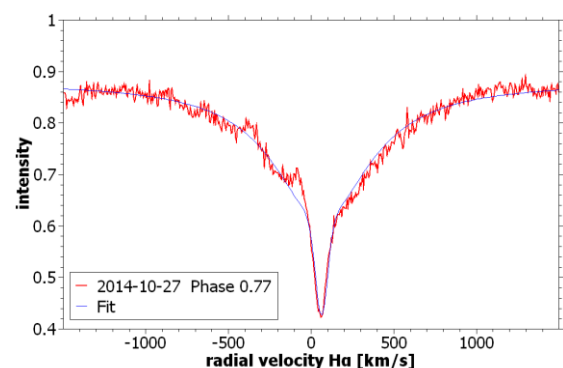
Fig. 3: Hα line of β Per at an orbital phase of 0.77 (red) and a pseudo Voigt fit (blue). A blue shifted emission occurs.

A corresponding spectrum recorded at phase 0.77 is shown in figure 3. At this orbital phase position an emission line can be seen with a radial velocity of (-83 ± 10) km/s. The primary star shows a red shifted radial velocity.

It can be concluded, that the emission region is moving synchronously to the K2 secondary star

around the mass center of the binary system (with a phase shift of 0.5 to the primary star), but with a significantly smaller radial velocity amplitude compared to that of the K2 component, which is 194 km/s (see table 1).

It is assumed that the emission structure originates from a hot spot in a gas stream from the K2 component to an accretion disc surrounding the primary star, forming a hot contact region. Indeed, such a hot spot region is described in detail in [6].

4. Investigation of the temporal stability of the emission structure

As the study of the hot spot in [6] is based on spectra from 1976/7, the temporal stability of the emission region after few decades since this investigation is an open question. We therefore present new measurements on the temporal variations of the emission structure in the following. Spectra covering a period of over one year were recorded. We then compare the Hα profiles taken at about the same orbital phase position.

Figure 4 shows such a series of spectra taken at phase positions between 0.2 and 0.3 and figure 5 gives the corresponding spectra for the phase positions of 0.7 – 0.8.

The green dotted line in figure 4 and the yellow dotted line in figure 5 indicate the position of the emission line. The emission line is visible in all of the presented spectra and seems roughly to be stable, no clear signs for temporal variations at the same phase are visible.

To extract the emission signature from the observed Hα absorption spectrum a corresponding pseudo Voigt fit as it is shown in the figures 1 – 3 was subtracted from each of the measured spectra. The resulting difference spectra are shown in the figures 6 – 9.

Fig. 6 shows the difference spectra for the orbital phase positions of 0.2 – 0.3 for the spectra shown in figure 4 recorded at observatory Bannewitz observatory. Additional data for the same phase position were taken by the Berlin observatory. The corresponding difference spectra of these data are shown in Fig. 7. The emission line is clearly visible in all of the difference spectra.
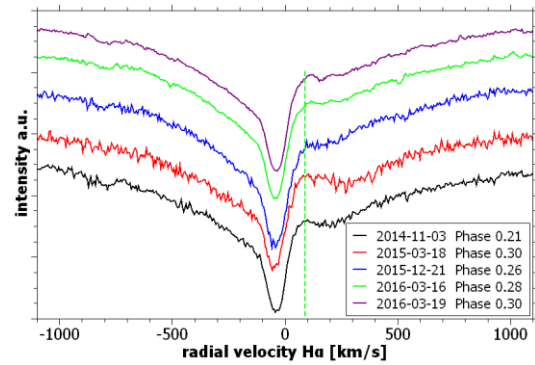
Fig. 4: Spectra of the Hα profile taken at phase positions of 0.2 – 0.3 from November 2014 until March 2016 from Bannewitz. The green line indicates the position of the emission line.
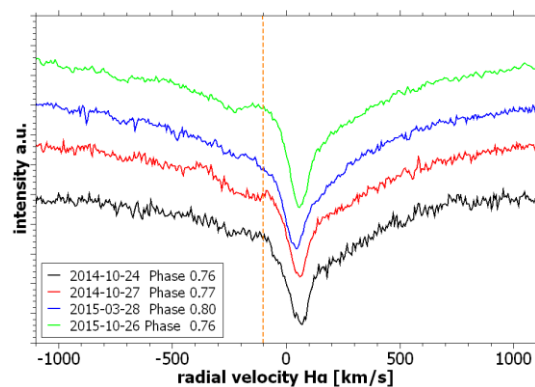
Fig. 5: Spectra of the Hα profile taken at phase positions of 0.7 – 0.8. The spectra from October 2014 until March 2015 were taken from Bannewitz and the profile from October 2015 from Berlin. The green line indicates the position of the emission line.

Fig. 6: Difference spectra of the measured Hα profiles from figure 4 and a fitted pseudo Voigt function. The emission line is clearly visible.

The details of the shape of the difference spectra depend strongly on the quality of the fit of the Hα absorption line. Because the pseudo Voigt fit is only a rough estimate of the real absorption line of the star, small structures in the difference spectra are expected being artifacts. The absorption like dip on the blue side of the emission line in figure 6 seems to be such an artifact, which is not visible in the spectra in figure 7.

Therefore, in the following, only the main emission peak in the difference spectra will be evaluated.

Fig. 7: Difference spectra of measured Hα profiles from Berlin and a fitted pseudo Voigt function. All spectra were taken in the orbital phase interval of 0.2 – 0.3 between September 29th and October 10th in 2015. The emission line is clearly visible.

Fig. 8: Difference spectra of the measured Hα profiles from figure 5 and a fitted pseudo Voigt function for the data from Bannewitz. The emission line is clearly visible.

The difference spectra for the orbital phase interval 0.7 – 0.8 calculated from the measured data in figure 5 are shown in the figures 8 and 9. Figure 8 shows the difference spectra of the data from Bannewitz and figure 9 the corresponding difference spectra for the data from Berlin.

Because the emission line is a very weak spectral signature, the difference spectra are very sensitive to the SNR of the raw spectra. The noise prevents the visibility of small temporal changes. Especially the spectra recorded from Bannewitz from 2014 and 2015, which were taken with the C8 telescope, with a SNR of about 100 – 150 achieved only relatively noisy difference spectra. For comparison, the spectra taken with the 16" RC telescope and an identical exposure time (green and violet curves in figure 4) showing a SNR of about 200 – 300 result in significantly less noisy difference spectra.

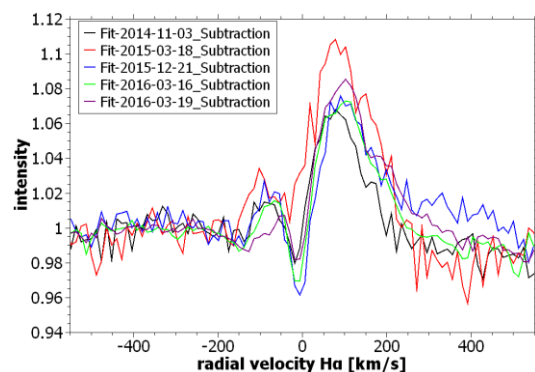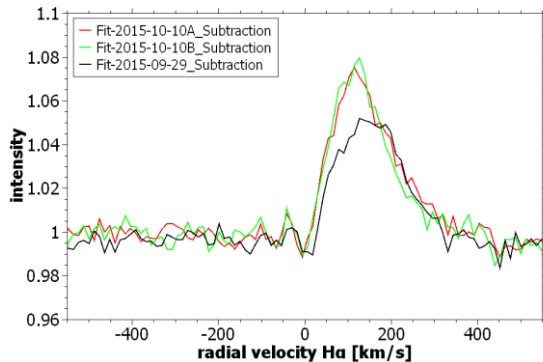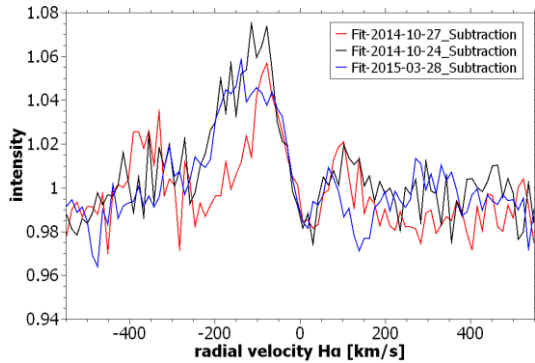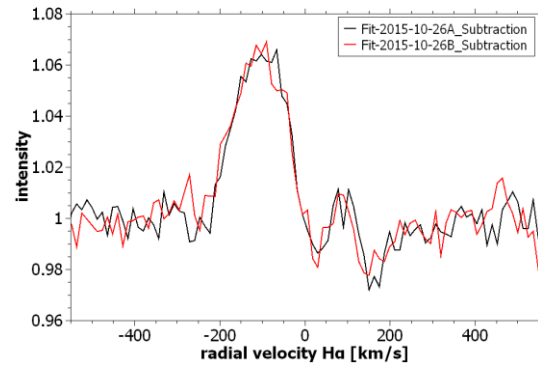**Fig. 9:** Difference spectra of the measured Hα profiles from Berlin and a fitted pseudo Voigt function. The emission line is clearly visible.

To investigate the temporal stability of the emission structure, the maximum of the main emission line in the difference spectra was determined by a Gaussian fit of the line. In addition, its equivalent width was measured. Table 2 shows the results for the spectra shown in figure 6 – 9.

Date (Observatory)	Phase	Max [km/s]	EW [Å]
03.11.14 (C8)	0.21	90	-1.7 ± 0.9
18.03.15 (C8)	0.30	102	-3.7 ± 1.9
10.10.15 (B)	0.22	133	-2.4 ± 0.8
21.12.15 (RC)	0.26	132	-2.2 ± 0.7
16.03.16 (RC)	0.28	138	-2.1 ± 0.7
19.03.16 (RC)	0.30	161	-2.7 ± 0.9
24.10.14 (C8)	0.76	-138	-2.0 ± 1.0
27.10.14 (C8)	0.77	-102	-0.9 ± 0.5
28.03.15 (C8)	0.80	-138	-1.7 ± 0.9
26.10.15 (B)	0.76	-120	-2.0 ± 0.7

Tab. 2: Radial velocity of the emission maximum in the difference spectra (Max) and equivalent width (EW) of the emission line. Obervatory: C8 spectra from Bannewitz with the C8, RC spectra from Bannewitz with the 16" RC and B spectra form Berlin.

The estimated error of the emission maximum due to the noise in the difference spectra is ± 50 km/s. The error of the equivalent width depends on the noise in the difference spectra and on the accuracy of the absorption line fit. It is estimated to be ± 50 % for the spectra taken with the C8, ± 30 % for the others and is shown in table 2.

In summary, the emission line is clearly visible during the whole observation period from October 2014 until March 2016. A significant variation cannot be noticed. The strength of the emission seems to be roughly constant within the measurement uncertainty.

5. Study of the orbit of the emission region

If the emission region stayed roughly stable during the observation period, an evaluation of the data as a function of the orbital phase could be carried out. The equivalent width and the radial velocity of the maximum of the emission line was determined for all the available difference spectra. The equivalent width as a function of the orbital phase is shown in figure 10. The error bars indicate the uncertainty in equivalent width as given in table 2. As already expected, the strength of the emission line shows maxima in the orbital phase intervals 0.2 – 0.3 and 0.6 – 0.8. An equivalent width of 0 indicates, that the emission is not visible at this specific orbital position.
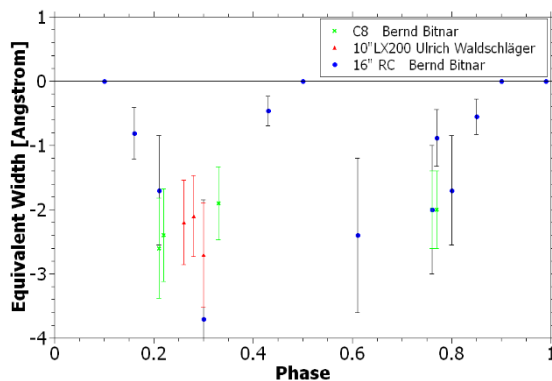

Fig. 10: Equivalent width of the Hα emission line as a function of the orbital phase, determined from the difference spectra in Fig. 6 – 9.

In figure 11 the radial velocity of the maximum of the emission line in the difference spectra is shown as a function of the orbital phase. The error bars indicate an estimated error in radial velocity of the emission maximum of ± 50 km/s.
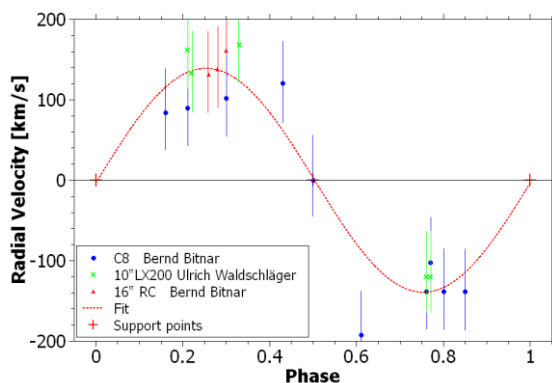

Fig. 11: Radial velocity of the Hα emission region as a function of the orbital phase, determined from the difference spectra in Fig. 6 – 9. In addition to the data from the measurements fixed data points are drawn for a radial velocity of 0 (red crosses). The red line gives a sinusoidal fit to the data.

If we suppose, that the emission region is located on the connection line between the two stars, it rotates in phase to one of the stars around the mass center of the system and its radial velocity is 0 for the orbital positions 0, ½ and 1. These three fix points are shown in figure 11 (red crosses) together with the measured data. Further, a sinusoidal curve is shown fitting the data together with the fix points.

A radial velocity amplitude of roughly 140 km/s of the emission structure has been determined from the sinusoidal fit. The radial velocity curve of the emission line is phase shifted by 0.5 to the primary star, which means it moves synchronously with the K2 secondary component around the mass center.

6. Discussion

The emission region moves synchronously to the secondary star around the mass center and shows a radial velocity amplitude of 140 km/s – about ¾ of the radial velocity amplitude of the K2 secondary component, which is 194 km/s. So, the origin of the emission is located relatively close to the secondary star - far away from the B8 primary star. If the emission occurs from a hot spot in a contact region between a gas stream from the K2 component and an accretion disc around the primary star, the accretion disc has a large extension.

In [6] images of β Per obtained with the Doppler tomography method [7] show that the conclusions from our data are roughly correct. The mass transfer in the binary system results in a hot spot located relatively close to the secondary component. The Doppler tomography analysis in [6] shows further, that the emission region is located relatively close to the connection line between the stars and that a second weaker emission region exists.

The main uncertainty in our analysis occurs due to the use of an empirical pseudo Voigt fit to the measured Hα absorption profile that is subtracted from the profile to obtain the difference spectra. Further, the average SNR of the data should be improved to reduce the noise in the difference spectra. It was already shown, that either by using a long exposure time as it was applied by the Berlin observatory or by using the large 16" telescope of the Bannewitz observatory the SNR could significantly be improved.

7. Summary and outlook

The Hα profile of β Per shows an emission line that was extracted from the measured absorption spectra by subtracting a simple pseudo Voigt fit. The analysis of the variation of the radial velocity of this emission line as a function of its orbital phase position points to the origin of the emission in a hot spot moving synchronously to the K2 secondary star around the mass center of the system. The emission region is located relatively close to the secondary star indicating a large extension of the accretion disc in the β Per system. This analysis and interpretation is in accordance with a detailed Doppler tomography study of β Per of Dunlap observatory from 1976/7 described ref. 6.

It remains an open question whether the hot spot in the accretion disc showed any variation since the last four decades. To answer this question a continued observation of the Hα emission structure of β Per is planned. To improve the accuracy of the evaluation it is projected to use a simulated model spectrum of the Hα absorption line instead of the simple pseudo Voigt fit. Further, the recording of additional spectra with an improved SNR is assigned for getting a deeper view into the geometrical details of the emission region in β Per.

References

[1] B. Bitnar, Spektrum 50 (2016) 20
[2] http://astrosurf.com/vdesnoux/
[3] http://www.peterschlatter.ch/SpectroTools
[4] V. Kolbas et al., arXiv:1506.01254v1 (2015)
[5] 9th Catalogue of spectroscopic binary orbits, http://sb9.astro.ulb.ac.be
[6] M. Richards et al, Astrophys. J. 459 (1996) 249
[7] T. M. Marsh et al., Mon. Not. R. Astron. Soc. 235 (1988) 269

Bernd Bitnar is a physicist, and professionally he is working in the development of solar cells. As an amateur astronomer, he has many years of experience in deep sky photography. In recent years, stellar spectroscopy from his own small observatory became a new astronomical challenge

The Mechanical Stability of Spectroscopic Setups, Part II

Jochem Berlemann
Horstweg 69, 32657 Lemgo, Germany, Email: jochem.berlemann@hs-owl.de

Abstract
In the first part of this paper we discussed the mechanical stability of the connection telescope/spectrograph case. In this second part, we examine the criteria for the stability of the spectrograph case itself. With simple preliminary FEA simulations we develop criteria for the final design. With Carbon Fiber Reinforced Plastics (CFRP) we get deflections of less than 1 µm for a load of 30 N (3 kg).

Zusammenfassung
Im ersten Teil dieses Beitrags haben wir die mechanische Stabilität der Verbindung zwischen Spektroskop und Teleskop diskutiert. In diesem 2. Teil untersuchen wir die Stabilität des eigentlichen Spektroskop-Gehäuses. In grundlegenden Voruntersuchungen werden Kriterien für den Bau steifer und leichter Gehäuse entwickelt. Die Anwendung dieser Kriterien erzielt bei Gehäusen mit einer Belastung von 30 N Gewicht (3 kg) Durchbiegungen von weniger als 1 µm. Karbon-Faser-Platten erweisen sich als das geeignete Material für unsere Anwendung.

1. Introduction

The mechanical stability of a spectrograph case depends on two properties of the applied materials: the intrinsic mechanical properties of the material and the geometrical shape of its parts. In the following we discuss both properties and develop design rules for a stiff and lightweight case. Two designs with deflections of less than 1 µm are proposed.

2. Behavior of Materials

2.1 Intrinsic Mechanical Properties

The two important mechanical properties for the materials in our design are the density ϱ and the Young´s Modulus E.

The density ϱ
The density ϱ of the material is measured in [g/cm³] and will give the mass *m* of a body in g when the volume is known. The weight of a body is a force – measured in N – which is applied to the mass *m* by gravity. Very often the name weight is used as a synonym for the mass *m*. For our design should ϱ be as small as possible as the weight of the mass will load the focuser of the telescope.

Young´s Modulus E
The Young´s Modulus – also known as the Elastic Modulus *E*, is a measure for the stiffness of a solid material [1]. The modulus *E* is measured

in Pa (Pascal), a unit of pressure (1 Pa = 1 N/m²). *E* describes the linear slope of the stress-strain-curve. The modulus *E should be as big as possible* to make a material stiff – this will be discussed below, see eq. 3.
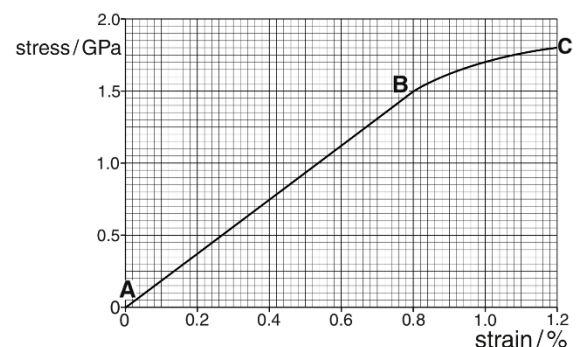
Fig. 1: Stress-Strain-curve. Stress is the applied force per unit area, strain is the relative elongation of the material due to the applied stress. The linear part is described by Hooke´s Law, source: ref. 2.

The slope of the curve between the points A and B – which is the elastic region in which we work – is steep for stiff materials.

Table 1 shows the density ϱ and the Young´s Modulus *E* of four materials as examples. Aluminum and CFRP (Carbon Fiber Reinforced Plastics) are well suited to be fabricated by astronomers with a moderately equipped mechanical shop. Titanium and Stainless Steel are listed for comparison.

Material	ϱ [g/cm³]	E [GPa]
Titanium	4.51	103
Stainless steel	8.0	193
Aluminum	2.7	69
CFRP	1.43	133

Tab. 1: Density ϱ and Young's Modulus E for four materials, source: ref 3.

Figure of Merit M_1

We can create a figure of merit M_1 for the materials to assess the suitability for our design: we denote the ratio of E to the density ϱ as M_1, its value should be as large as possible.

$$M_1 = \frac{E}{\rho}$$

(1)

Table 2 shows the ratio M_1 for the materials in table 1.

Material	M_1 [GPa cm³/g]
Titanium	22.6
Stainless steel	24
Aluminum	25.5
CFRP	95

Tab. 2: Figure of merit M_1 of the material from table 1.

Clearly the CFRP is by far the best suitable material for our design, followed by Aluminum.

2.2 The Geometrical Shape of Components: Second Moment of Area

Creating stiffness by a suitable geometrical form of the components is another aim of our design for the spectroscopic case.

Rectangular Cross Section

One important property for the stiffness of a component is the Second Moment of Area I (or Moment of Inertia) which is defined by the geometry of the beam. I should be as large as possible for a good stiffness. For our example of a rectangular cross section, it can be calculated to [4]:

$$I = \frac{bh^3}{12}$$,

(2)

b is the width and h the height of the beam according to fig. 2.

Exemplarily, values for a beam of certain dimensions are summarized in table 3. The force applied is always directed perpendicular to b into the direction of h (top down in fig. 2).
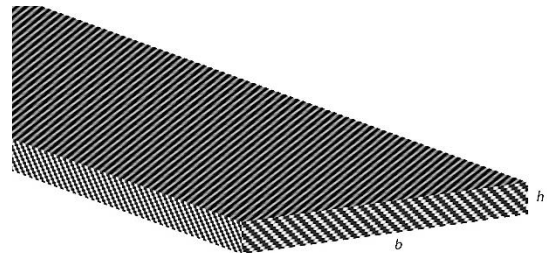
Fig. 2: Cross section of a rectangular bar with notations of dimension b and h from table 3.

b	h	I	A
10	30	22500	300
30	10	2500	300
5	30	11250	150
30	5	312	150
10	100	833333	1000
100	10	8333	1000

Tab. 3: Second Moment of Area I and cross sectional area for different rectangular bars. The width b and height h are in mm, I in mm⁴ and the cross-sectional area A in mm².

For a large value of I it is much more favorable to apply the force alongside the longer side of the bar (for the same area (weight)). We can increase I and hence the stiffness by increasing the width b and the height h of the beam. Both measures will increase the mass of the beam, too – but the increase of h acts with the power of 3 in eq. (2)! The increase of the beam height h is favorable over the width b when improving the stiffness of the component.

T-Cross Section

For a beam which is reinforced by a bar according to fig. 3 some values of I are calculated in tab. 4. The formula for the calculation is more complicated than (2). It can be found in [5]. We used an online calculator [6] for getting the values in tab 4.

Fig. 3: T-Cross section with dimensions used in table 4.

B	H	b	h	I	A
100	10	5	40	15181	1200
100	10	10	20	7000	1200
100	5	5	40	11201	700
100	5	8	25	6425	700

Tab. 4: T-cross section. All bar dimensions as in fig. 3 are in mm, I in mm^4 and the cross-sectional area A in mm^2.

For a desired large value of I it is favorable to make the perpendicular reinforcement bar thin and high.
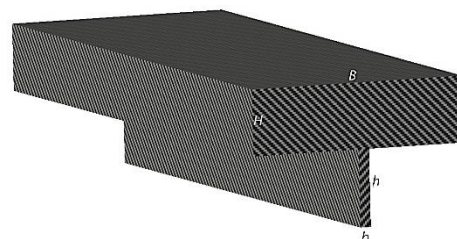
2.3 Summary of Material Properties

For a lightweight, stiff mechanical design the value of the density ϱ should be as small as possible, the values of E and I as large as possible.

3. Deflection $u(x)$

3.1 Notations and coordinates

At this point we have to express the notations of variables and coordinates more rigorously than in part 1 of this paper: the coordinate system we use can be found in fig. 4.
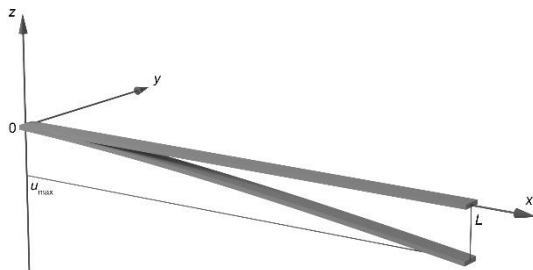

Fig. 4: Coordinate system.

We apply the forces into the negative z-direction. The deflections into the negative z-direction are notated as $u(x)$. Their values depend on the coordinate x along the beam and are negative, as well. For simplicity, we list the deflections into the negative z-direction $u(x{=}L) = u(L)$ with their absolute values in the following tables.

3.2 The Cantilever Beam

To calculate the influences of ϱ, I and E on the deflection $u(x)$ we now have a look onto a thin rectangular Cantilever beam of length L (Fig. 5).

This beam is loaded by the weight of the material (represented by ϱ or q) and by a force F at the free end. The other end is assumed fix. Both

deflections can be calculated separately and added.
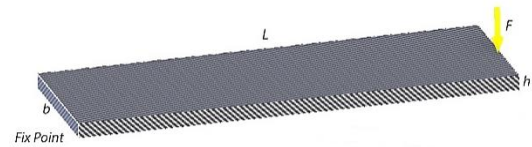
Fig. 5: Cantilever beam of length L=300 mm, width b and height h.

3.3 Deflection by Force F

The deflection $u(L)$ of a weightless, thin beam at the end at location L where a point force F is applied can be calculated by a differential equation. For our simple geometry, the solution of the equation can be written as [9]

$$u(L) = -\frac{FL^3}{3EI} \tag{3}$$

E is again the Young´s Modulus and I is the Second Moment of Area.

3.4 Deflection by weight q

The deflection of a thin beam due to its weight can be calculated again by a differential equation. For our geometry, we get a simple solution in the form, see appendix and [8, pp. 102],

$$u(L) = -\frac{qL^4}{8EI} \tag{4}$$

q is here the specific weight of the material of the beam and is measured in [g/mm]. To minimize the deflection due to bending we gather from (3) and (4) that E and I should be as large as possible as stated above.

4. FEA Simulations for Deflections

To get quantitative results for deflections with different parameters discussed before, we may now have a look onto the simple Cantilever beam in fig. 5. The beam of length L is loaded by a force F at the end.

4.1 The Thickness of a Rectangular Cantilever Beam

We have loaded a Cantilever beam of different thicknesses and materials with a load force F of

100 N into the minus z-direction at the end (that equals a mass m of approx. 10 kg). The other end is fixed. The weight of the materials has been included into the simulations. Table 5 shows the deflection $u(L)$ (bending) at the end of the beam in µm and the mass m of the bar. The length L is 300 mm and the width b is 100 mm in all simulations.

Material	h	$u(L)$	m	M_2
Al	10	1296	0.807	1041
Al	20	163	1.61	262
Al	30	49	2.43	119
Ti	10	858	1.35	1158
Ti	20	108	2.7	291
Ti	30	32.6	4.05	132
CFRP	10	659	0.428	280
CFRP	20	83	0.857	71.1
CFRP	30	25	1.29	32.2

Tab. 5: Simulation results of the maximum deflection $u(L)$ for different materials and thicknesses h. For explanation of M_2 see text below. h is measured in mm, $u(L)$ in µm, m in kg and M_2 in kg µm.

Second Figure of Merit M_2

To evaluate the best combination of geometry and mass for our design we calculated another figure of merit M_2. M_2 is the product of mass m and the maximum deflection $u(L) = u_{max}$ and it should be as small as possible.

$$M_2 = m \cdot u_{max} \tag{6}$$

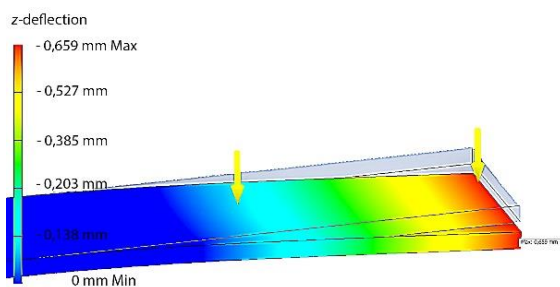Fig. 6 shows the result of the simulation with CFRP and a thickness $h = 10$ mm.

Fig. 6: Deflection z for a simple cantilever beam with CFRP as the material. The thickness h is $h = 10$ mm.

From the explanations above we now understand why the CFRP-beam of 30 mm thickness gives us the best tradeoff between weight and deflection - ϱ is low, E and I are large. The value of M_2 is 32.2 kg µm.

4.2 Direction of the Force

To simulate the influence of the direction of the force we compare the simulation of the Cantilever beam from fig. 5 with the simulation according to fig. 7: $L = 300$ mm, $b = 100$ mm, h = 10 mm and the material is Aluminum. The weight has been included in the simulation directing into the same direction as the force F into the horizontal direction.
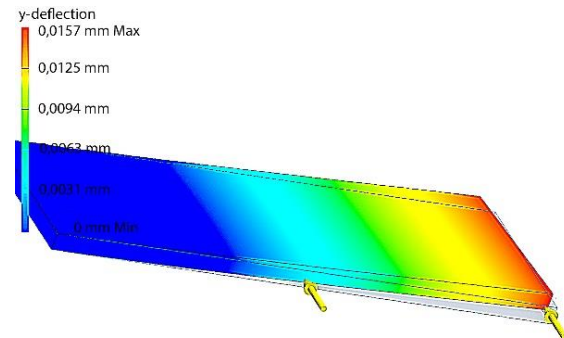
Fig. 7: Deflection by weight and the external force F applied both into the horizontal y-direction.

The deflection is reduced from 1296 µm to 15.7 µm just by changing the direction of the forces. The reason is the significantly increased value of I due to the interchange of h and b in eq. 2.

4.3 Trade-Off Between Mass and Deflection

In the next step, we reduce the mass m of the Aluminum beam with $h = 30$ mm, $b = 100$ mm, $L = 300$ mm by drilling out some holes (fig. 8). The holes were applied towards the free end of the bar where the material has little stress.
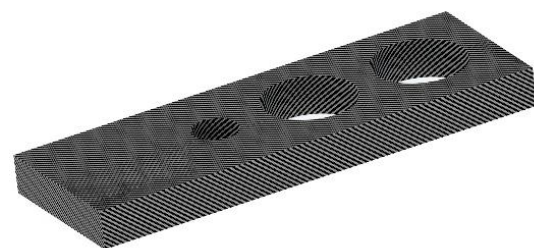
Fig. 8: Beam of fig. 2 with holes reducing weight.

As expected, the mass m is reduced, but the deflection increased. Thus, the value for M_2 is decreased by this measure. Table 6 shows the results of this simulation for Aluminum and CFRP.

It is important for the stiffness to apply the holes in a region without large stress (e.g. near the free end).

Material	*u(L)*	*m*	*M₂*
Solid Al bar	49	2.43	119
Al with holes	58.3	1.91	111.3
Solid CFRP bar	25	1.29	32.2
CFRP with holes	29.8	1.01	30.1

Tab. 6: Simulation results of the maximum deflection $u(L)$ for beams with and without holes and two different materials. $u(L)$ is measured in µm, m in kg and M_2 in kg µm.

4.4 Reinforcement Plate Added

Fig. 9 shows the stress in the material. The bending emerges in the region of big stress (red and blue color). Hence, we reinforce the thickness of the wall with an additional plate near the fix point according to fig. 10. We get from our simulations the results according to table 7.
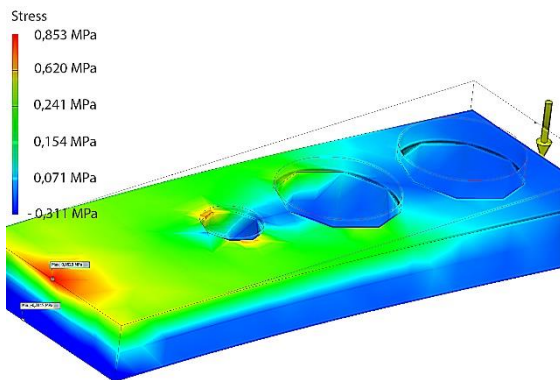

Fig. 9: Stress plot of the bar with holes. The stress in the material is at maximum near the fix point.
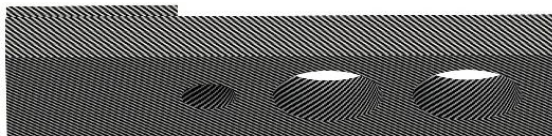

Fig. 10: Additional reinforcement plate at the fix point.

Material	*u(L)*	*m*	*M₂*
Al, fig. 9	58.3	1.91	111.3
Al, fig. 10	39.3	2.15	84.5
CFRP, fig. 9	29.8	1.01	30.1
CFRP, fig. 10	20.1	1.14	22.9

Tab. 7: Simulation results of the maximum deflection $u(L)$ for beams with and without reinforcement plate and two different materials. $u(L)$ is measured in µm, m in kg and M_2 in kg µm.

We gain some stiffness by adding weight. The figure of merit M_2 decreases positively.

4.5 The T-Shape

In the next step, we try to improve the stiffness of the component shown in fig. 5 by adding a reinforcement bar along the line of bending according to fig. 11. Table 8 shows the results for $B = 100$ mm, $H = 10$ mm, $b = 5$ mm, and $h = 40$ mm.
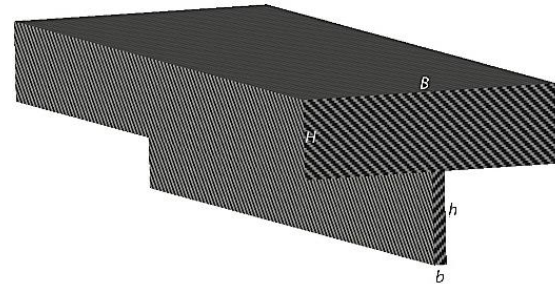
Fig. 11: A reinforcement bar along the line of bending adds stiffness (T-shape bar).

Material	*u(L)*	*m*	*M₂*
Al, fig. 5	1296	0.807	1041
Al, fig. 11	86.2	0.97	83.6
CFRP, fig. 5	655	0.428	280
CFRP, fig. 11	44.2	0.514	22.7

Tab. 8: Simulation results of the maximum deflection $u(L)$ for beams with and without perpendicular reinforcement bars (T-shape bars) and two different materials. $u(L)$ is measured in µm, m in kg and M_2 in kg µm.

By adding a reinforcement bar, we increase the Second Moment of Area I. With this measure, we add moderate weight but decrease the deflection by a big amount. This is the effect of shape stability.

4.6 Twisting of plates

Up to now we have discussed the bending of plates only. Bending appears in our design more often as the so-called twisting where two forces in opposite directions act onto a component. To give an idea how twisting can be avoided we first simulate a situation of twisting of the beam by two forces (fig. 12).

Fig. 13 shows a measure against that twisting. The results are shown in table 9 for CFRP. It seems from the results that reducing the twist is more difficult than to reduce some bending.

Material	*u(L)*	*m*	*M₂*
Beam, fig. 12	± 66.8	0.81	54.1
Beam, fig. 13	± 22.7	1.46	33.1

Tab. 9: Deflection z is reduced by reinforcement bars as seen for $u(L)$. $u(L)$ is measured in µm, m in kg and M_2 in kg µm.

Fig. 12: Twisting of the beam by two opposite forces of 100 N. The main deflection appears into *z*-direction – the direction of the forces.

Fig. 13: The effect of shape stability reduces the twisting into the *z*-direction.

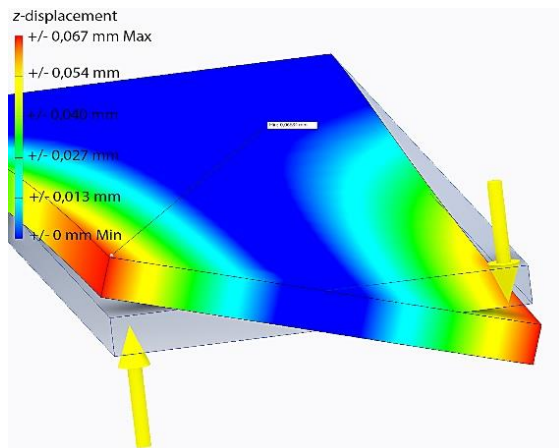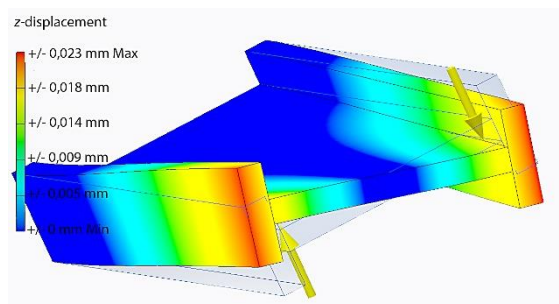### 4.7 Summary of basic simulations

If we want lightweight stiff components we have to use CRFP as the material. Aluminum behaves worse but is better than Stainless Steel or Titanium. It is better to use the effect of shape stability than adding material to add stiffness because that spares significant additional weight. Nevertheless, the material near the fix point should be more solid as at the rest of the case. We can save weight by removing material in regions with less stress.

5. Final Simulations of a Case

5.1 Sim No. 1, Fig. 14, Basic Case

With these results in mind we simulate spectrograph cases. The starting point is the basic case we already simulated in Part 1 of this paper – see fig. 14. Here we had a maximal *z*-deflection of 119.7 µm – which was unacceptable large.

We improved this design by considering the following points:
- CFRP as the material and
- Stable fix point with a 68-mm thread.
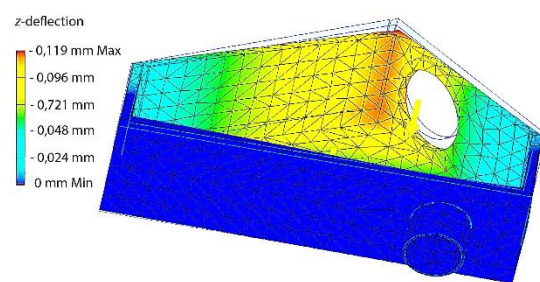
Fig. 14: Deflection of old design, the basic case from part 1 of this paper.

The result is a modified case design according to fig. 15. The interface to the scope is a thread of 68 mm (the fix point) which is a standard in astronomic equipment. The guiding head has been incorporated into the case. The whole region around the fix point is more solid as in fig. 14. A cover plate stabilizes the side walls, the side walls stabilize the bottom plate where the optical components are applied. The thickness of all plates is 5 mm. The load is given by the weight of the material and a force *F* of 30 N (or mass equivalent 3 kg) by the objective/camera.
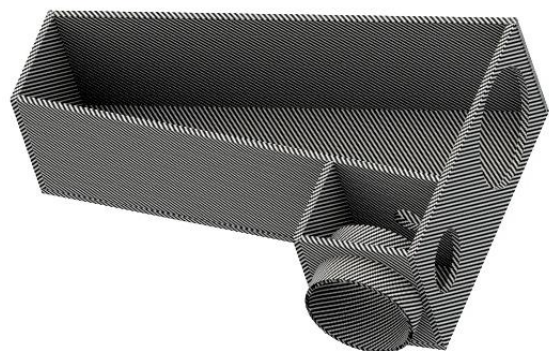
Fig. 15: Basic case for simulation No. 1 with top cover plate (not shown here). Functional holes for telescope connection, guiding camera, camera objective and a passage for the beam between the two chambers are visible.
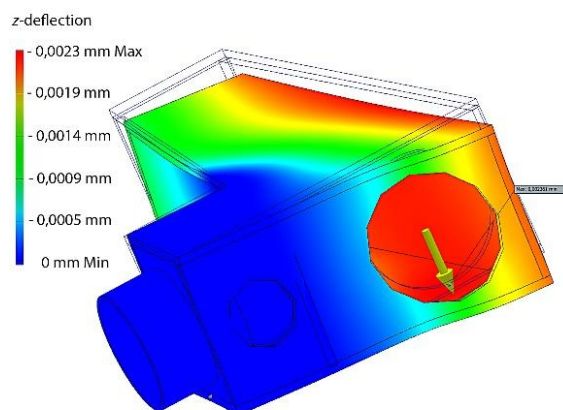
Fig. 16: *z*-deflection of simulation No. 1, the basic case of fig. 15.

The results of this simulation are a mass m of 1.3 kg and a maximum deflection of 2.36 µm into the negative *z*-direction. Fig. 16 shows the deflection, fig. 17 the stress in the material for this situation.
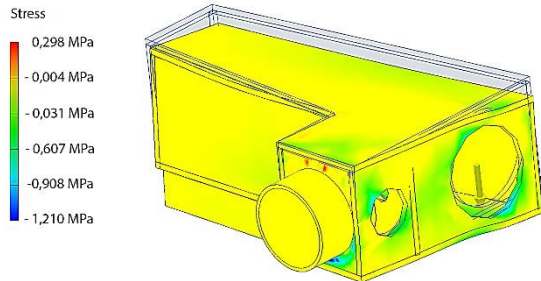
Fig. 17: The mechanical stress in the material. Yellow means little stress, Red and Blue means large stress. The nose is the fix point.

The most detrimental bending for our application occurs in a line between the fix point (nose with M68 thread) and the load of the camera and objective. The largest stress occurs around the M68 nose and the location of the load.

5.2 Sim No. 2, Fig. 18, Added Stiffness

First, we add a L-shaped plate around the nose and along the main line of bending. The thickness of this additional plate is 10 mm. Furthermore, we fix a reinforcement stripe of 10 mm thickness along the side plate with extraordinary bending at the edge (fig. 18). As expected the mass increases from 1.3 kg to 1.7 kg and the maximum deflection decreases from 2,4 µm to 1,0 µm by these measures.
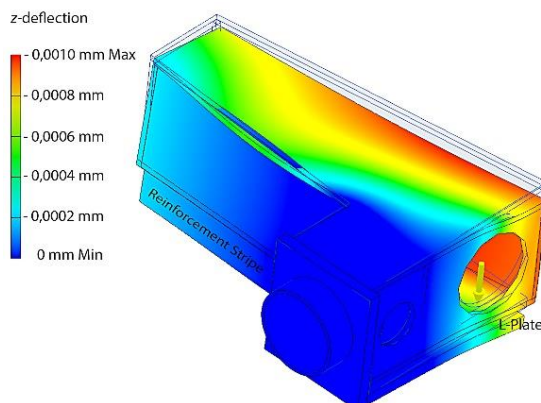
Fig. 18: *z*-deflection of simulation No. 2, the case with structural improvements for stiffness increase.

5.3 Sim No. 3, Fig. 19, Reducing Mass

To reduce the load for the focuser we drilled holes in regions where little stress is applied to the material (fig. 19).
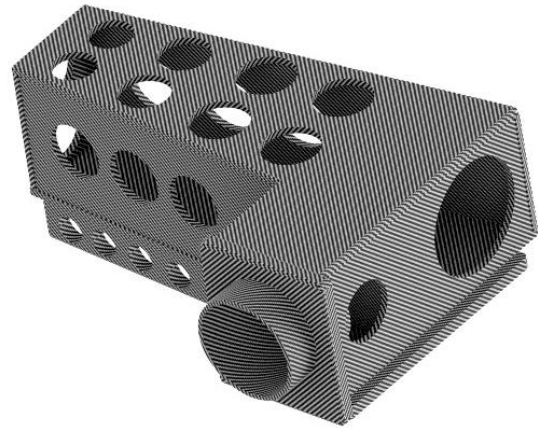
Fig. 19: The design for simulation No. 3 with reduced mass.

By this measure we reduce the weight to 1.53 kg, the deflection increases to 1.26 µm. The figure of merit M_2 increases a little. This option could be taken if the mass is decisive.

5.4 Sim No. 4, Fig. 20, Alternative Design

As an alternative solution, we added according to fig. 20 three reinforcement stripes and one plate at the nose to the starting configuration of fig.15. All new parts have a thickness of 10 mm.
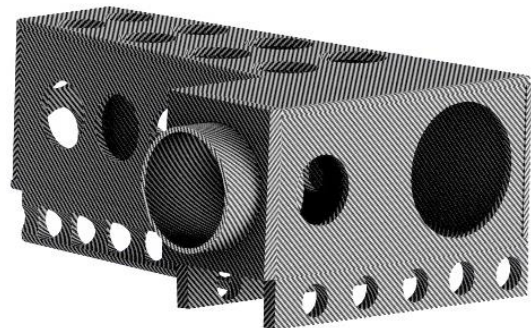
Fig. 20: Alternative design to increase the stiffness of the basic layout of fig. 15. The mass is reduced by holes.

We get a maximum deflection of 1.29 µm with a mass *m* of 1.32 kg by this means.

5.5 Summarized Results

In table 10 we summarize the results of the simulations for CRFP. We also added the results of Aluminum as an alternative material for comparison if the costs are to be reduced or preventing risks of fabricating with CRFP, respectively.

Sim No	Config.	u_{max}	u_{Obj}	m	M_2
old	Fig. 14 Part 1	119	90	2.79	332
1a	Fig. 15 CRFP	2.4	1.6	1.3	3.12
1b	Fig. 15 Al	6.4	3.7	2.29	14.6
2a	Fig. 18 CRFP	1.0	0.5	1.7	1.7
2b	Fig. 18 Al	2.6	1.7	3.11	8.1
3a	Fig. 19 CRFP	1.26	0.6	1.53	1.93
3b	Fig. 19 Al	3.4	1.4	2.81	9.55
4a	Fig. 20 CRFP	1.29	1.0	1.32	1.7
4b	Fig. 20 Al	3.4	1.2	2.41	8.2

Tab. 10: Summary of simulation results. M_2 is calculated from u_{max}. The deflection at the location of the objective u_{Obj} is estimated from the color scale in the simulation plots. u is measured in µm, m in kg and M_2 in kg µm.

6. Discussions

We developed two alternative designs to get a good stiffness and a small mass for our spectroscopic case. The mass m of the case has been considered by calculating a figure of merit M_2 which is the product of the maximum z-deflection and the mass m. M_2 should be as small as possible. If the stiffness is decisive one should take the CRFP design of fig. 18 or fig. 19. If the total weight is important, the design of fig. 20 is recommended. Aluminum as a material is a good low cost alternative for most applications.

The design has been chosen in such a way that everyone equipped with a good semiprofessional mechanical shop can build it. If one uses CRFP health protections have to be taken into account.

There may be further little improvements with the application of more sophisticated simulation tools. The program *Hyperworks* with the module *Optistruct* by Altair [7] can optimize the design of fig. 20 by removing material in an alternative way than drilling simple holes. It creates a sort of framework – but this is much more difficult to produce. In any case the stiffness of the whole spectroscopic setup can be improved by the measures described in Part 1 of this paper.

Appendix

Comparison of mathematical and technical methods to determine the deflection of a Cantilever Beam
by Marietta Ehret and Jochem Berlemann

As we were interested in the basics of the elasticity problems we encountered, we examined the solutions of differential equations, FEA simulations and a mechanical measurement.

1. Comparison of FEA Simulation with Measurements

We compared a FEA simulation of a Cantilever Beam with a mechanical measurement. The simulation gave a result of 295 µm for the maximum deflection. The mechanical measurement resulted in a deflection of 315 µm. The difference can be explained by a little flexion in the fix point of the mechanical setup.
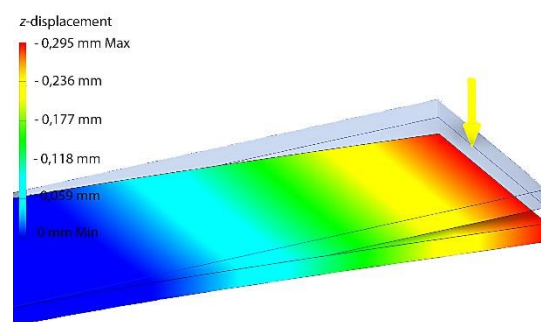
Fig. 21: Deflection in the simulation for a Aluminium beam with length L = 300 mm, width b = 100.28 mm, height h = 8.25 mm. The external Force is F = 12.85 N.

There is a good coincidence between the FEA simulation result and the reality. Another argument to trust the simulations is the so-called Authority Proof. Thousands of engineers using FEA for buildings, bridges, cars and other things simply can´t be wrong.

Fig. 22: Mechanical setup for the deflection measurement. One small unit on the dial gauge corresponds to 10 µm. The result has been checked with a caliper gauge, as well.

2. Analytical solutions of differential equations

Taking a mathematical point of view – especially a geometrical one, we discuss the solutions of the corresponding elasticity problems. This may seem easy, but it is a highly complicated mathematical problem.

Let as consider a thin beam, where thin means, that its profile area is small with respect to its length L. The shape of its profile does not play an important role. We put this into a 2-dimensional coordinate system (x,z) and denote the deflection by u, see fig. 23.
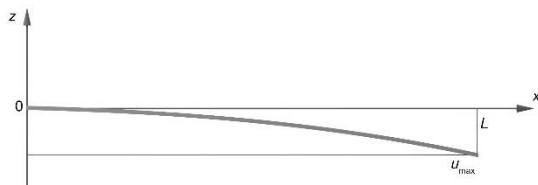
Fig. 23: The 2-dimensional coordinate system with a thin beam of length L. The deflection is denoted by u, its maximum shall be u_{max}. The thin beam is fixed at the zero-point 0.

In the case of the thin beam and if the force F and the weight act only into the z-direction we can neglect the consideration of the perpendicular y-direction. Thus, function u depends only on x in space: $u = u(x)$.

In our setting, we are interested in solutions of elasticity problems where we have the weight of the bar itself. Additionally, we have a force F at the free end of the beam by other components (camera, objective). Both results can be superimposed.

Case 1: Deflection by own weight

If we denote the specific weight of the beam per length by q, we find the solution of the elasticity problem

$$\frac{d^4u}{dx^4} = -\frac{q}{EI}$$

with the boundary conditions

$u(0) = 0$
$u'(0) = 0$
$u''(L) = 0$

in an analytic way

$$u(x) = -\frac{q}{24\,EI}\,x^2(x^2 - 4Lx + 6L^2)$$

see [8, p. 102 f.].

The beam is simulated in comparison. There is a very good coincidence between simulation and analytic calculation. The shapes $u(x)$ fit very well. The simulation gives a deflection $u(L)$ = 46.1 μm, the analytical solution of the differential equation gives $u(L)$ = 46.4 μm.
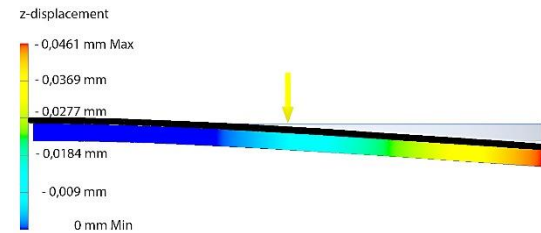
Fig. 23: Results of FEA simulation (beam with colored displacement) and the solution of the differential equation (black line). The yellow arrow indicates the weight as the load in the simulation and the analytic solution and is evenly distributed over the length of the beam, of course. Geometry: L = 300 mm, b = 100 mm, h = 10 mm. The material is Aluminum.

Case 2: A force F at the free end of the beam as a boundary condition

According to Landau the differential equation reads

$$\frac{d^3u}{dx^3} = -\frac{F}{EI}$$

with boundary conditions for u as in case 1. By integrating one finds the analytic solution:

$$u(x) = \frac{F}{6EI}\,x^2(x - 3L)$$

[8, p. 103]. For $x = L$ one gets the solution

$$u(L) = -\frac{FL^3}{3EI}$$

which is now very well known by a lot of other authors, e.g. ref. 9 and 10.

A critical remark

Unfortunately, the solution taught worldwide does not meet the simulation results and the reality exactly. We checked that the analytical results are about 10 % bigger than the results of the corresponding simulations. The reason is simple: the force F is represented by a Dirac

Operator δ. In Landau's textbook the problem is circumvented by formulating the condition "... along the whole beam the force F is constant…" [8, p. 103].

We can correctly formulate the differential equation for our problem as

$$\frac{d^3u}{dx^3} = -\frac{F\delta(x-L)}{EI}$$

with the same boundary conditions as in case 2. Here, δ(*x-L*) is the Dirac Operator which represents the point source *F* at the position *x=L*. But we cannot find explicit analytic solutions for this differential equation. For an analytical solution of the kind

$$u(x) = \sum_i a_i x^i$$

the third derivation *u'''*(*x*) – which vanishes for all x ∈ (0,*L*) but not in *x* = *L* – does not exist.

FEA simulations avoid this problem of singularities by using discrete geometric elements (finite elements) and discretization instead of differential equations [11].

References
(all web references from 2017-04-10)

[1] https://en.wikipedia.org/wiki/Young's_modulus
[2] http://i-want-to-study-engineering.org/figs/as_2013_g481_physicsa_m_q8iii.png
[3] http://www.autodesk.com/products/inventor/overview
[4] https://en.wikipedia.org/wiki/Second_moment_of_area
[5] http://www.engineersedge.com/material_science/moment-inertia-gyration-6.htm
[6]:http://civilengineer.webinfolist.com/str/micalct.php
[7]:http://www.altairhyperworks.com/product/optistruct
[8] L. D. Landau; E. M. Lifschitz: Lehrbuch der Theoretischen Physik, Bd. 4: Elastizitätstheorie, Akademie-Verlag Berlin, 1975.
[9] http://www.me.berkeley.edu/~lwlin/me128/BeamDeflection.pdf
[10] http://ocw.nthu.edu.tw/ocw/upload/8/258/Chapter_9-98.pdf
[11] Eriksson, K. et. al.: Angewandte Mathematik: Body and Soul, Band 2 und 3, Springer Heidelberg, 2013

Jochem Berlemann was Professor at the University of Applied Sciences OWL for 26 years. His fields were Communication and Media Techniques. He is now retired and has enough time for the fascinating hobby of astronomy. Please follow the link www.darkskyfriends.de.

Solar Imaging with a Spectroheliograph: Part 1

Peter Zetner

556 McAdam Avenue, Winnipeg, Manitoba, R2V 0A9, Canada, Email: p_zetner@hotmail.com

Abstract

A spectroheliograph (SHG) is an imaging spectrograph used to photograph the Sun at a selected wavelength with narrow spectral bandpass. This paper gives a brief historical introduction to the development of the SHG and describes the design and utilization of an amateur-built instrument. The device has been designed to give full disk solar images (~2000 x 2000 pixels) and has been operated with a spectral resolving power of $R \sim 74000$. Example images taken by setting the SHG wavelength to various Fraunhofer absorption lines are presented. Strikingly different aspects of the solar atmosphere (photosphere and chromosphere) are observed depending on the choice of wavelength. In addition to imaging, scientific studies of photospheric and chromospheric motions, active region magnetic fields, prominence velocity distributions and other subjects are possible, some of which are discussed in the paper. The design and construction of such an instrument are well within the capabilities of a motivated amateur.

Zusammenfassung

Ein Spektroheliograph (SHG) ist ein abbildender Spektrograph zur Aufnahme der Sonne bei verschiedenen Wellenlängen. Dieser Artikel gibt einen kurzen historischen Rückblick auf die Entwicklung der SHG und beschreibt das Design und die Anwendung eines Selbstbauinstrumentes. Das Gerät ist für die Abbildung der gesamten Sonnenscheibe (~2000 x 2000 Pixel) konstruiert und bietet eine spektrale Auflösung von $R \sim 74000$. Beispielbilder, die bei Wellenlängen der Fraunhoferlinien aufgenommen sind, werden dargestellt. Verschiedene auffällige Eigenschaften der Sonnenatmosphäre (Photosphäre und Chromosphäre) werden in Abhängigkeit der gewählten Wellenlänge beobachtet. Neben der Abbildung werden einige weitere Untersuchungen wie die photo- und chromospärischen Bewegungen, magnetische Felder aktiver Gebiete, Geschwindigkeitsverteilungen von Protuberanzen diskutiert. Der Entwurf und die Konstruktion eines solchen Instrumentes liegt im Bereich der Möglichkeiten des ambitionierten Amateurs.

1. Introduction

The spectroheliograph (SHG) is a device which captures an image of the Sun at a well-defined centre wavelength, in a very narrow spectral passband, by utilizing a prism or grating spectroscope for spectral dispersion. It was developed independently by George Ellery Hale and Henri-Alexandre Deslandres in 1890, ref. 1 and references therein. The motivation for the development of such an instrument can be read from the paper of Hale and Ellerman [2]. "The application of the spectroscope in 1868 to the observation of solar prominences in full sunlight opened an extensive field of research, and directed the attention of astronomers to the importance of applying the powerful instruments and methods of the physical laboratory to the study of the Sun. Since that time, the rise and development of stellar spectroscopy have further emphasized the importance of solar investigation."

The "application of the spectroscope in 1868 to the observation of solar prominences in full sunlight" to which Hale refers is the method employed by Huggins [3] where light from the solar limb was imaged onto the entrance slit of a spectroscope tuned to an absorption line of hydrogen. Prominences were revealed as bright emission features and some of their spatial characteristics could be resolved by widening the spectroscope slits. Hale set out to improve this method so that more spatial information about the prominence could be revealed while preserving the spectral purity.

Quoting again from Hale and Ellerman [2]: "A first step in this direction was attempted by the invention of the spectroheliograph in 1889. The original purpose of this instrument was the photography of the chromosphere and prominences, in order to simplify and render more accurate the daily delineation of their form. It was

subsequently found ... that the instrument had a far wider range of application, and that it could be applied in directions which had not suggested themselves in 1889."

With his spectroheliograph at the Mount Wilson Observatory, Hale pursued the "far wider range of application" and discovered the calcium intrachromospheric network (ICN) and the presence of a double reversal in the CaII H and K lines. Hale's early imaging studies were limited to the blue and UV spectral regions. However, the development of improved red sensitive photographic emulsion by R. J. Wallace in 1908 led to his work with Hα spectroheliograms which revealed the highly-structured hydrogen chromosphere and led to his discovery of "vortices" around sunspots which he correctly attributed to the action of magnetic fields. Using high dispersion spectrographs, he was one of the first to observe line splitting and polarization effects (near sunspots) in accordance with Zeeman's laboratory experiments and went on to measure field strengths and polarities for hundreds of sunspots by 1920, introducing a classification scheme which exists to this day.

During Hale's long illness (he died in 1938) the Mount Wilson spectroheliograph was dedicated to the rather routine acquisition of Hα and CaII K line images. Further innovation in the use of the instrument awaited the work of another pioneer and innovator, Robert Leighton and his group at the California Institute of Technology [4,5]. Leighton and coworkers developed techniques to produce spectroheliograms whose intensity variation is sensitive to the Doppler and Zeeman effects. They were successful in mapping velocity and magnetic field distributions in the solar atmosphere. The work of Leighton is mentioned in this introduction because, as will be seen below and in part 2 of this article, Doppler imaging and magnetic field mapping is within the grasp of the amateur solar astronomer with the use of a SHG!

The above gives a short, historical introduction to the development of the SHG. Instruments of this type are still in use in modern solar research, perhaps, most importantly, in space based observatories. For example, a primary imaging instrument of the Solar Dynamics Observatory, launched in 2010, is the extreme ultraviolet (EUV) multiple wavelength spectroheliography [6]. More recently, the IRIS (Interface Region Imaging Spectrograph) instrument, launched in 2013, will produce high resolution (spectral and spatial) solar images in the ultraviolet [7].

2. Design and Operation of an Amateur-Built SHG

Much of the SHG work of Hale and others was carried out at the hydrogen alpha wavelength (6562.8 Å) and the calcium K line (3933.7 Å). The interest in these two particular wavelengths arises from the fact that light emanating from these very strong spectral (absorption) lines originates, largely, from the solar chromosphere, a layer of the Sun in which the dominating influence of magnetic fields on the gas dynamics produces a wealth of complex structures of great scientific interest and beauty.

In recent years, there has been growing interest, on the part of amateurs, to pursue solar imaging by spectroheliography. As described below, this pursuit has become much easier with the development of video imaging techniques. The recent book by Harrison [8] gives an overview of amateurs employing the modern technique of "digital" spectroheliography. An advantage of the SHG, even in the age of readily available Hα and Ca K narrowband filters, is its spectral selectivity (bandpass). This is determined by the spectroscope and associated optics and can be made (almost) arbitrarily narrow, at least much narrower than the passband of most commercial filters. The wavelength of observation is usually chosen to coincide with a spectral line of one of the solar chemical elements, most frequently, but not exclusively, selected to be a strongly absorbing line of a chromospheric constituent, like the hydrogen or calcium lines mentioned above. In fact, tunability of the SHG to a desired wavelength presents a huge advantage over fixed wavelength filters and allows one to explore the additional techniques of doppler imaging and magnetic imaging.

As an introductory description of the operation of the SHG, I've chosen to quote the early paper by Hale (Hale, 1903): "The principle of the spectroheliograph is exceedingly simple. Imagine a direct-vision spectroscope in which the eyepiece ordinarily employed is replaced by a (second) slit. If an image of the Sun is formed on the first slit of this spectroscope, the second slit will permit the passage of only a narrow region of the spectrum corresponding in width to this slit. If the (second) slit is now moved until it coincides with the H beta line, for example, only hydrogen light will pass through the instrument. If, then, a photographic plate is placed behind and almost in contact with the second slit, and the spectroscope is moved at right angles to its optical axis, an image of the Sun, in monochromatic hydrogen light, will be built up on the plate from the successive images of the slit. If the ex-

posure is suitable, the chromosphere and prominences will be shown surrounding this image. Such is the spectroheliograph in its simplest form. It is obviously immaterial whether the motion be given to the spectroscope, on the one hand, or to the solar image and photographic plate, on the other. It is only necessary that the relative motion of the solar image and first slit be such that light from all parts of the solar disk shall pass successively through the slit, while the photographic plate and second slit experience a corresponding relative motion. The second slit serves simply to isolate any desired line in the spectrum; hence its width must be such as exactly to include this line, and to exclude all light from other parts of the spectrum."

A point worth emphasizing is the required relative motion of solar image with respect to the first slit and synchronized relative motion of the second slit and photographic plate. In the Rumford spectroheliograph, set up by Hale at Yerkes Observatory and operating by 1903, scanning of the Sun's image across the primary slit was accomplished by a uniform motion of the telescope tube in right ascension while the photographic plate was being moved at the same time and rate across the secondary slit. Another example is an improved instrument set up at the Royal Observatory, South Kensington, UK, in 1905 and used extensively by William Lockyer [9]. This instrument made use of a scheme in which both the solar image in the focal plane and the photographic plate remained fixed in position while a moving platform housing the spectrograph, comprising entrance slit, exit slit and dispersing optics, was translated laterally with a precisely controlled hydraulic piston.
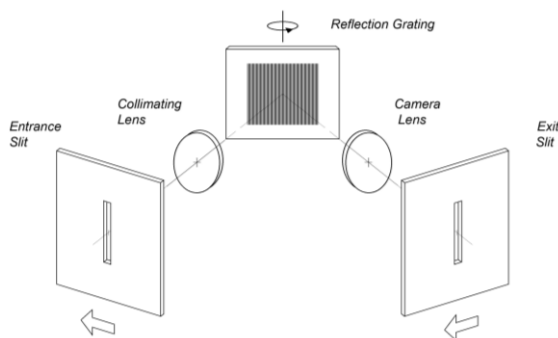

Fig. 1: Generic diagram of a spectroscope with reflection grating as the dispersive element. The axis above the grating, with circular sense defined, indicates the method of tuning the spectroscope. The arrows show scanning directions used in the early SHG instruments of Hale, Deslandres and others.
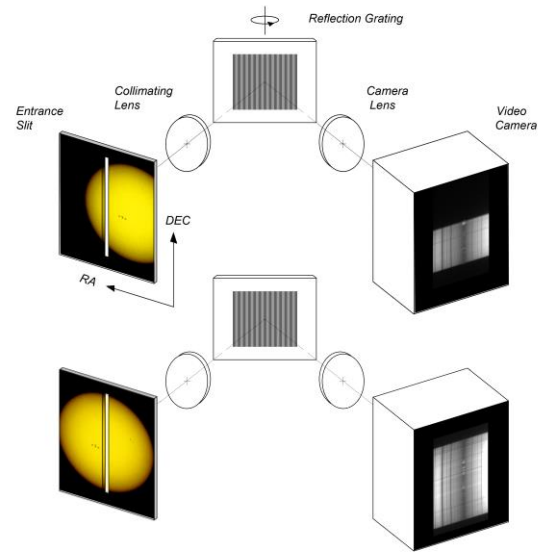

Fig. 2: Operating principle of a modern spectroheliograph. The solar disk at two possible positions on the entrance slit during its drift is shown along with the two corresponding video frames. In any given video frame, spectral information is encoded along the dispersion direction (roughly horizontal in the figure) and spatial (image) information is encoded perpendicular to the dispersion direction (vertical in the figure) contained in the corresponding slice of the solar disk present at the entrance slit.

Figure 1 presents a schematic diagram of a typical spectroscope lying at the heart of these early instruments. The dispersive element in this case is a reflection grating whose direction of dispersion is perpendicular to the long dimension of the slits. By locating the (narrow) entrance slit at the telescope focal plane, a sharp solar image falls on the slit. The entrance slit also lies in the focal plane of the collimator lens such that rays emanating from any given source point in the entrance slit are transformed, by this lens, into a parallel bundle of rays incident on the grating at a direction determined by the location of the source point. This parallel bundle of rays is reflected by the grating, in the dispersion direction, by an amount dependent on the wavelength of the light. For some particular wavelength, these reflected parallel rays intercept the camera lens and are brought to a focus at the (narrow) exit slit. The particular wavelength of light at which this happens can be selected by rotating the grating about the indicated axis, allowing the device to be "tuned". Any source point in the entrance slit is brought to a corresponding image point at the exit slit but with wavelength-selected light. Since the solar disk is imaged at the entrance slit, a corresponding monochromatic image of the portion of the disk occupying the entrance slit is generated at the exit slit. The exit slit image can be magnified or de-magnified by adjusting the ratio of camera lens to collimator lens focal lengths. The "spectral purity" of the light transmitted

through the exit slit is determined by the entrance and exit slit widths, the focal lengths of collimator and camera lens and the grating dispersion (determined by the number of grooves per unit length). The spectral purity increases (ie. the spectral bandpass narrows) with decreasing slit width, increasing focal lengths and more grooves per unit length. The arrows drawn below the entrance and exit slits in figure 1 indicate the direction in which the scanning takes place, solar image scanned across the entrance slit in synchronism with the photographic plate scanned across the exit slit.

Strictly speaking, the device described in the preceding lines is a "monochromator". Multiwavelength (polychromatic) light passes the entrance slit and (nearly) monochromatic light emerges from the exit slit. By removing the exit slit and replacing it with a camera film or sensor plane, a "spectrograph" is configured. The wavelength dependent directions of reflected light from the grating transform, via the camera lens, into wavelength dependent positions on the sensor plane: a spectrum is generated.

If we now take the spectrograph camera and replace it with a video camera, we have configured the modern SHG. The scanning required to produce images with the SHG is inherent in the video camera and can be almost trivially simple to implement. The telescope is pointed in a fixed direction along the Sun's path and the solar image allowed to drift across the entrance slit, which is oriented such that the dispersion direction corresponds to right ascension (RA). Video is acquired at the camera frame rate, each video frame capturing a spectrum associated with the particular slice of solar disk present at the entrance slit at the moment the frame is exposed. The general scheme is shown in figure 2 with the solar disk illustrated at two possible positions on the entrance slit and the two corresponding video frames. In any given video frame, spectral information is encoded along the dispersion direction (roughly horizontal in the figure) and spatial (image) information is encoded perpendicular to the dispersion direction (vertical in the figure) contained in the corresponding slice of the solar disk present at the entrance slit.

At this point it is tempting to imagine that the camera frame rate (in frames/second: fps) should be carefully matched to the solar drift rate in order to achieve the required synchronization. However, there is no stringent requirement whatsoever on the frame rate, aside from ensuring it is greater than a minimum value. The minimum frame rate, fps_{min} is determined by the solar disk diameter, D, at the entrance slit, the entrance slit width, w, and the transit time of the

complete disk across the slit, T (= 127.6 s). The required calculation is:

$$fps_{min} = (D / w) / T.$$

The minimum frame rate ensures that no portion of the solar image is lost to the imaging process in the dead time between video frames. Experience has shown me, however, that image quality increases with increasing frame rate. The instrument described below comprises a 1000 mm telescope and, most commonly, an entrance slit of 25 microns width. The minimum frame rate for this configuration would be 2.9 fps. A 15 fps video capture is generally used, "oversampling" the spatial information at the entrance slit by a factor of 5.
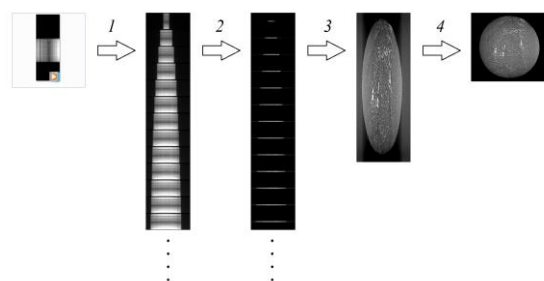

Fig. 3: Illustration of the procedure required to form an image from the video file acquired during a solar disk drift scan. Images from left to right represent: the video file, the sequence of video frames ready for editing, the sequence of cropped video frames, the concatenated assembly of cropped video frames and the final spectroheliogram. Steps 1 through 4 are described in the text.

The procedure required to form an image from the video file acquired during a solar disk drift scan is represented in figure 3. The video file is loaded into video editing software in step 1. My preference is the VirtualDub program [10]: freely available and versatile. In step 1, a rotation of the video of 90 degrees (CW) is shown, not necessary for image processing but convenient for the purpose of drawing the figure! Keep in mind that, with the indicated rotation, the dispersion direction in figure 3 is vertical (as opposed to, roughly, horizontal in figure 2). Close inspection of the 2nd (from the left) image in figure 3 shows that each video frame covers the same spectral region, in this particular example, near 393 nm, chosen by tuning the grating appropriately. Dark bands running horizontally are the various spectral absorption lines present in this region of the solar spectrum. The rather wide, fuzzy spectral line in the center of each frame is the strong CaII K absorption line at 393.37 nm. The variation in intensity along the CaII K line, from left to right in any given frame, contains the spatial (image) information in this particular slice of the solar disk due to the intensity variation of the CaII K absorption across the slice. The visible bright spots, for example, are

generally associated with regions of chromospheric plage. Note the presence of thin vertical lines in the spectra. These lines ("transversalium") are associated with dust and irregularities on the entrance slit. In step 2, each frame of the video is cropped to isolate a single spectral line of interest, the CaII K line in the example. In a sense, this step introduces a "digital" exit slit such that the final image will represent the solar disk viewed at a single wavelength. It must be noted that the spectra shown in figure 3 are somewhat idealized. In most instruments, the recorded spectral "lines" have some curvature associated with them ("smile") and may be rotated somewhat in the frame.

Step 2, therefore, generally involves video frame image processing in addition to the cropping. Fortunately, VirtualDub has a number of video filters available which can be used to remove smile and rotation from each video frame. I have found the "General Quadrilateral Transform", "Barrel Distortion" and "Rotate2" filters to be especially useful. Once the spectral lines have been straightened by filtering, the cropping can be applied. The location of the crop (i.e. the vertical height of the crop within the frame, in figure 3) will determine the wavelength at which the final image is constructed and the width of the crop will determine the spectral bandwidth. For reasons discussed below, I generally choose the cropping to isolate a strip of 2-pixel width in order to minimize the bandwidth. In some cases, enlarging the crop width is useful, especially in the imaging of solar prominences. Once each frame has been suitably cropped, the cropped frames need to be assembled (concatenated) to produce the solar disk image. This is represented by step 3 in the figure. In my processing workflow, step 3 involves exporting the cropped frames, as a sequence of separate images, to a folder using the VirtualDub "Export" command. Assembly of these individual images into a single image is carried out with ImageJ, another freely available image processing package which is well known to many astronomers. The commands "Import > Image Sequence" followed by "Image > Stacks > Make Montage" achieve the (nearly!) desired result, the 4th image from the left in figure 3. The image resulting from concatenation of the cropped video frames in step 3 is, invariably, elongated by an amount dependent on the camera frame rate and the chosen pixel width of the crop. The elongation can be easily corrected by adjusting the aspect ratio in any image processing software. This adjustment alleviates the need to enforce a stringent synchronization between camera frame rate and solar image drift rate since it, essentially, takes an average over redundant, oversampled frames. The tremendous simplification afforded by this image processing correction is a luxury that early spectroheliographers like Hale and Deslandres were unable to enjoy! Step 4 represents this correction along with other image enhancements like contrast and sharpness adjustments. At this point, it is also desirable to remove the transversalium lines mentioned above. This can be painstaking and difficult, depending on the severity of the problem, but can be accomplished by various filtering actions. I use Adobe Photoshop and ImageJ to finalize the image.
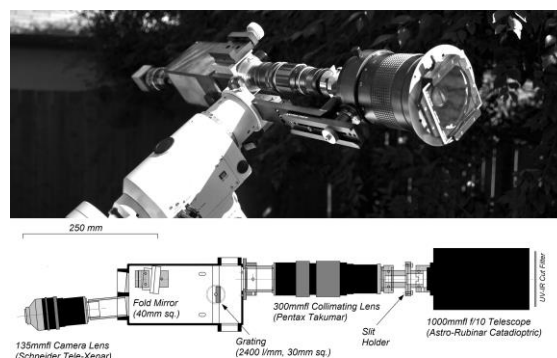

Fig. 4: Schematic diagram and photograph of the instrument. It is shown attached to an NEQ-6 mount.

The names of a number of amateur astronomers, who have pioneered the development of the modern SHG as described above, come to mind: Andre and Sylvain Rondi, Phillipe Rousselle and Daniel Defourneau. Information about their work is available online and they, along with others, are profiled in Harrison's book [8]. A photograph and schematic diagram of the SHG I have constructed is given in figure 4. The instrument is built around a surplus Czerny-Turner spectrograph housing which was modified by introducing a hole and flange to accept incident light from the direction shown. The basic design philosophy was to incorporate M42 camera lenses (readily available on eBay) to provide the collimation and focusing. These lenses are often well-corrected for aberrations (notably Pentax Takumars) and come in a large variety of focal lengths giving some versatility to the design. Coupling between the various lenses is accomplished with combinations of step adapter rings as well as T-mount adapters. In the interest of keeping the device relatively small and maneuverable, an "Astro Rubinar" f/10 lens (100 mm aperture), of catadioptric (Maksutov) design, is used as the telescope. To protect the cemented achromats located near the focal plane of the catadioptric telescope, a uv-ir blocking filter (Schneider True-cut, 100 x 100 mm²) has been mounted in front of the telescope objective.

The telescope produces a solar image of approximately 9.3 mm in diameter which is focused onto a 25 µm x 18 mm long slit held in place by a modified version of the original spectrograph slit holder. A collimator focal length ranging from 300 mm to 750 mm has been used in various versions of the instrument. Longer focal lengths of collimator are desirable as they give a smaller angular magnification of the solar disk (less vignetting at the grating) and an increase in the spectral resolving power. On the other hand, the longer the collimator focal length, the slower the optical speed (f/#) of the system. At 300 mm, the collimator gives an angular magnification of 3.3x in combination with the 1000 mm telescope, corresponding to a 1.7° angular divergence of the beam illuminating the grating and an optical speed of f/10 (30 mm square grating) at the spectrometer input. This is an ideal match to the f/10 telescope lens and fixes the overall system speed at f/10. Also, for this collimator focal length, a spectral resolving power of approximately 20,000 is achieved with 25 µm slit and 2400 l/mm grating.

The final diameter of the solar image at the camera is related to the solar image diameter at the entrance slit by a magnification factor, m, determined by the ratio of camera to collimator focal length;

$$m = f_{cam} / f_{coll}.$$

For the configuration shown in figure 4 ($f_{coll} = 300$ mm, $f_{cam} = 135$ mm), $m = 0.45$ and the solar image size at the camera is 4.2 mm. This is a reasonable match to the 1/3" CCD sensor size (5.80 x 4.92 mm²) of the Imaging Source DMK31AU03 camera used in my first imaging efforts. The same magnification factor, m, determines the image slit width at the camera sensor. For $m = 0.45$ and a slit width of 25 µm, the slit image width is 11.3 µm (2.4 pixels for the DMK31AU03). This image slit width of 2.4 pixels underlies the rationale for cropping slices of 2 pixels width out of the video frames as discussed above. It is also consistent with the Nyquist criterion for digital sampling applied to the spatial information contained within each slice.

3. Some Example Images

Figure 5 shows "portraits" of the solar disk obtained in eight different wavelengths (in this case, over two observing sessions). This figure demonstrates the beauty of using the SHG to capture an image of the Sun in almost any wavelength of interest, at high spectral resolution. We can see that there are vast differences in the appearance of the solar disk at different wavelengths. Chromospheric structure is evident in such spectroheliograms of strong lines taken with high spectroscopic resolution. As discussed, for example, by Foukal, the structure observed arises from heights in the solar atmosphere where the selective optical depth is unity [11]. Figure 6 summarizes, in graphical form, the distribution of these "line formation heights" in the solar atmosphere with height = 0 (photospheric surface) defined by a condition on the optical line depth at 500nm wavelength: $\tau_{500nm} = 1$. Additionally, the plotted curves show the generally accepted variation of temperature with height given by the VAL model of ref. 12.
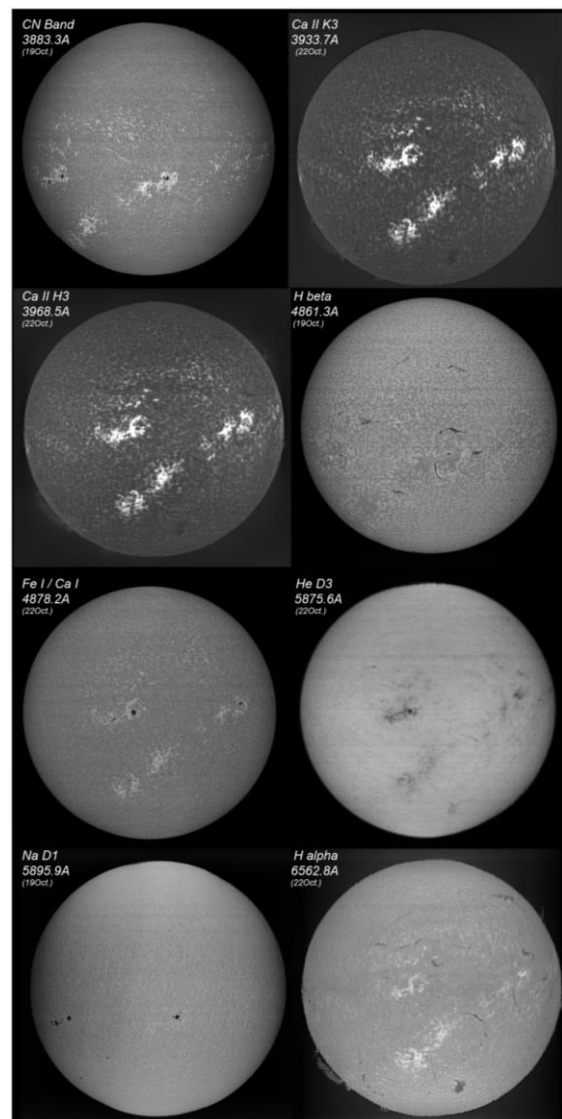

Fig. 5: Solar disks imaged in eight wavelengths on 19 Oct 2015 and 22 Oct 2015. The spectral bandwidth is approximately 0.025 nm. 1000 mm f/10 Rubinar, 500 mm collimator lens, 2400 l/mm grating, 300 mm camera lens; Pt. Grey Grasshopper, 6.0 Mpx.

For images taken in the centers of the Hα and Ca K, H lines, these heights correspond to the high chromosphere (1300 km < h < 2000 km).

Such images are dominated by the intense light from chromospheric plage which correlates with active regions of high magnetic field on the solar surface. Prominences and filaments are clearly visible in these particular images. The Ca K and H line images also clearly show the bright mottled pattern associated with the intrachromospheric network (ICN).

For Hβ, Hγ and the line wings of Hα and K lines the mid chromosphere (300 km < h < 1300 km) is visible. The Hβ image in figure 5 shows the ICN as a dark mottled pattern. Filaments are quite visible. Prominences are visible as well for these spectral lines, but require more processing and higher gain to image properly.

The low chromosphere / high photosphere (h < 300 km) is imaged in the centers of other strong (e.g. metallic) lines. In this region near the photospheric surface, many Fraunhofer lines weaken in active regions. This happens because of the required balance between the sum of magnetic and gas pressures inside an active region with the gas pressure of the non-magnetic surroundings [13]. The line weakening manifests itself as a local brightening in spectroheliograms at the line cores and, consequently, photospheric, "facular" regions can be mapped with high contrast in some metallic lines (Fe I, Ca I) and some molecular bands (CH, CN). The facular regions on the solar surface correlate in location with the chromospheric plage.

Some metallic-line spectroheliograms show, outside the facular plages, coarse dark "mottles" correlated with the ICN clearly seen in the Ca H, K lines. The contrast of these mottles increases as one moves out from the line center to the steeply rising Doppler wings, reaching a maximum about three Doppler widths from the line center, and then decreases again to zero in the damping wings. This can be interpreted as a result of local Doppler shifts and is, in fact related to the motions of supergranules on the solar surface. This pattern of mottles can be seen in figure 5 for the spectroheliogram taken in Na D light. This image was produced at a wavelength slightly to the blue side of Na D line center.

Figure 5 also shows a chromospheric image of the Sun in the light of the He D_3 line which is not well described by the discussion above [14]. This line is generally invisible on the solar disk (absorption is too weak) except in regions of plage and filaments where absorption is slightly enhanced. For this reason, the He disk is difficult to image. My technique involves making a series of SHG images at different wavelengths near D_3. One of these images is selected as representative of the nearby continuum and this

image is subtracted from the others in the series to reveal (hopefully) absorption features. By trial and error, choice of the correct image to subtract can be made by looking for the highest contrast in the resulting absorption features.
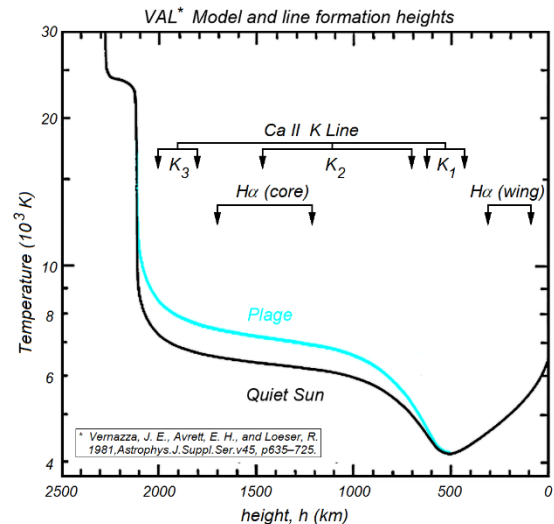

Fig. 6: (Adapted from ref. 11) The distribution of line formation heights in the solar atmosphere. Different wavelengths within the broad, doubly reversed Ca II K absorption line are identified by the notation K_1, K_2 and K_3. K_3 denotes line center, K_2 denotes the line reversal at line center ± ~0.015 nm and K_1 denotes the second line reversal at line center ± ~0.03 nm. Plotted curves show the generally accepted variation of temperature with height given by the VAL model of ref. 12.
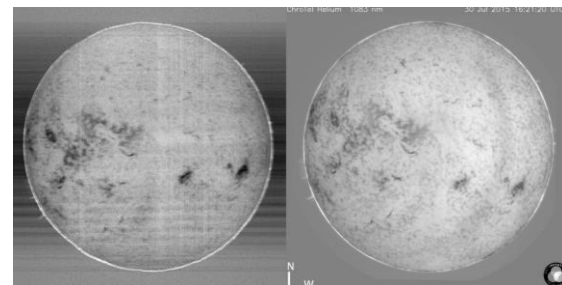

Fig. 7: Solar disk imaged on 03 Jul 2015 in the He D_3 absorption line (left) and a comparison image (filtergram) from the Kiepenheuer Institut fur Sonnenphysik (KIS) ChroTel telescope imaged in the He 1083nm infrared line (right).

The correlation between He D_3 absorption features and Hα features can be seen in Figure 5. The line is very bright at the limb and in prominences. There is a bright D_3 limb "band" visible in telescopes with very high angular resolution. Measurements show that this band corresponds to He D_3 emission from a shell with a sharply defined lower edge about 1400 km above the photosphere. The mechanism of He D_3 absorption is interesting. Extreme ultraviolet (EUV) radiation from the corona shines downward, illuminating neutral He from above. This EUV light is energetic enough to ionize the He. Recombination of the ions and free electrons

then produces neutral He in excited states of high excitation energy (~20eV) from which we see absorption at the D_3 line as well as the He IR (10830 Å) line. The observed shell in limb emission is consistent with this idea. The bottom of the shell corresponds to the maximum depth that the coronal EUV radiation can penetrate (downwards). Also, because radiation from the corona is required, He D_3 absorption features don't appear where coronal holes are present. He IR images are used as "proxy" maps of coronal holes, the only tool to map coronal holes from the ground. He D_3 images could serve the same purpose but the D_3 absorption is much weaker than the IR absorption.
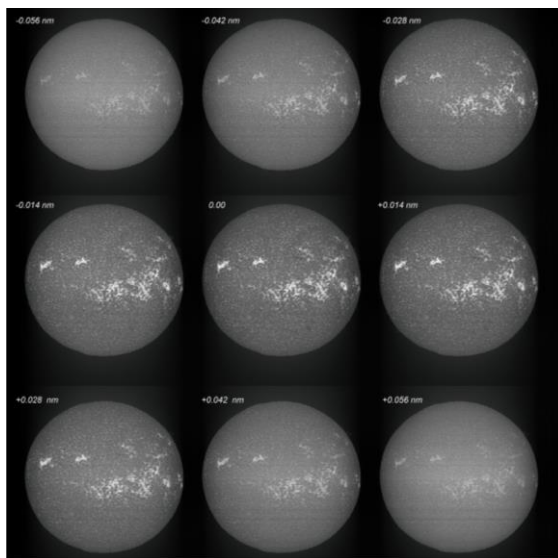

Fig. 8: A spectral series of images of the solar disk through the Ca K absorption line. The frames in these images are labelled by the wavelength offset (in nanometers) from observed line center.

Figure 7 presents a comparison of one of my He D_3 spectroheliograms with a professional He 1083 nm IR filtergram of the ChroTel telescope by Kiepenheuer Institut für Sonnenphysik (KIS) [15]. There is a very good correspondence between absorption features on the solar disk observed at the D_3 and IR wavelengths. Prominences are also clearly visible at both wavelengths.

In spectroheliograms of strong absorption lines, like Ca K and Hα, it is correct to say that images produced at wavelengths further away from line center reveal the solar structure at lower heights in the atmosphere, until we reach the continuum where the photospheric surface is imaged. This tendency is also shown in figure 6. The SHG lends itself easily to the generation of images at different wavelengths and, therefore, it is relatively simple to reveal the solar disk structure as a function of height in the solar atmosphere. In Figure 8, I present a "spectral series" of images

through the Ca K absorption line. The frames in this figure are labelled by the wavelength offset from line center. Such series can be interpreted as a study of the "tomography" of the solar atmosphere, different frames representing different heights. In figure 8, for example, one can see several sunspots visible, near the west limb of the solar disk, for the upper left and lower right frames. These frames are far enough in the wings of the Ca K absorption line that they are dominated by photospheric structure, hence the sunspots are clearly visible. However, in the center frame at line center, there is very little evidence of the spots. This image is dominated by upper chromospheric structure, particularly filaments, bright plage and the ICN. Spectral series of images can also be effectively displayed as animations. A spectral sweep through the Ca K line is available:

http://www.astrobin.com/101287/0/?nc=user

Other than wavelength diverse imaging, the SHG allows detailed study of velocities of solar features, magnetic field effects and more, making for an extremely interesting technique accessible to the amateur. Some of these topics will be discussed in a forthcoming article. Here, I present, in Figure 9, a spectral series of images of solar prominences. Our viewpoint for these features is quite different than our viewpoint of the solar disk because, rather than observing the solar atmosphere "top down" we are observing the chromosphere in emission and in profile. The striking difference in prominence shapes observed in such a spectral series of images is now due to the Doppler effect associated with line-of-sight motion of the prominence plasma. It is straightforward to identify regions of plasma which are moving toward or away from us at some specified velocity using the Doppler formula:

$$\Delta\lambda / \lambda = v / c,$$

where $\Delta\lambda$ is the wavelength offset from line center (λ), v is the line of sight velocity of the plasma imaged at the offset $\Delta\lambda$ and c is the vacuum speed of light. For the Ca K spectral series given in figure 9, an offset of $\Delta\lambda = 0.01$ nm from line center corresponds to a line of sight velocity of 7.6 km/s, with a positive (+) offset identifying recession and a negative offset (-) identifying approach. Note that the wavelength offsets quoted in figure 9 are determined with respect to the center of the absorption line peak as observed in the SHG. Hence the velocities extracted from these offsets are given with respect to a stationary Sun in that the rotation of the Sun is ignored. Using a calibration spectrum from a terrestrial source would allow determination of the velocities with respect to an Earth observer,

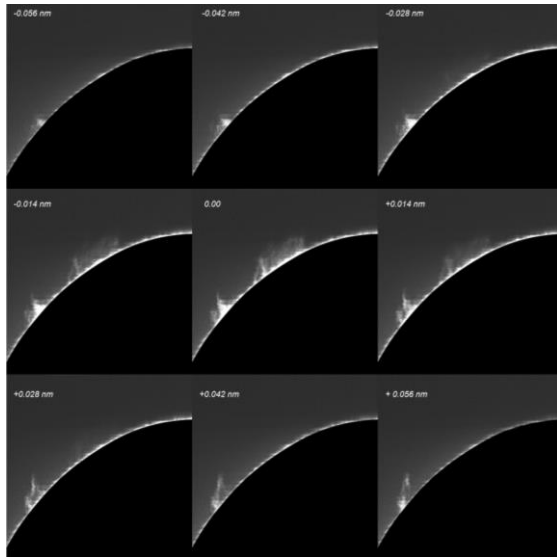but I have not yet made use of such a calibration scheme.

Fig. 9: A spectral series of images of prominences at the solar limb through the Ca K absorption line. The frames in these images are labelled by the wavelength offset (in nanometers) from observed line center.

The SHG described here is in a, more or less, continual state of flux. The modularity inherent in the design allows for straightforward re-configuring of the optics. A planned measurement of magnetic fields, for example, will require the introduction of polarizers which is relatively straightforward to accomplish. In addition to the fascination of imaging the Sun in light of high spectral purity, I find much additional enjoyment in this ability to modify the instrument itself.

References

[1] J. Hearnshaw, "Astronomical Spectrographs and Their History", Cambridge University Press, (2009)
[2] G. E. Hale and F. Ellerman F., "The Rumford Spectroheliograph of the Yerkes Observatory", Publications of the Yerkes Observatory V3. Pt1, University of Chicago Press, (1903)
[3] W. Huggins, Proceedings of the Royal Society, 17 (1869) 302
[4] R. B. Leighton, R. W. Noyes and G. W. Simon, "Velocity Fields in the Solar Atmosphere, I. Preliminary Report", ApJ 135 (1962) 47
[5] R. B. Leighton, "Observations of Solar Magnetic Fields in Plage Regions", ApJ 130 (1959) 366
[6] sdo.gsfc.nasa.gov
[7] www.nasa.gov/mission_pages/iris/index.html
[8] K. Harrison, "Imaging Sunlight using a Digital Spectroheliograph", Springer "Practical Astronomy" Series, (2015)
[9] W. Lockyer, "The Spectroheliograph of the Solar Observatory", MNRAS 65 (1905) 473L
[10] www.virtualdub.com
[11] P. Foukal, "Solar Astrophysics", Wiley-VCH Verlag GmbH & Co. KGaA, (2013)
[12] J. E Vernazza, E. H. Avrett and R. Loeser, " Structure of the Solar Chromosphere. III - Models of the EUV brightness Components of the Quiet Sun", ApJ Suppl. Ser. 45 (1981) 635
[13] H. Uitenbroek and A. Tritschler, "Narrow-band imaging in the CN band at 388.33 nm", A&A 462 (2007) 1157
[14] H. Zirin, "Astrophysics of the Sun", Cambridge University Press (1988)
[15] www.leibnitz-kis.de/en/observatories/chortel

Peter Zetner is a retired physics professor from the University of Manitoba, Canada. He spent 28 years teaching and pursuing his research interests in the laboratory study of laser-excited atomic collisions. He has had a lifelong interest in amateur astronomy and now has the time and means to explore this hobby in detail. At the moment, his special interests are "spectroheliography" and solar imaging. He plans to devote time to stellar spectroscopy in the near future with instruments currently under design and construction.

Beobachtung der Lutetium II – Linie bei 6222 Å auf der Sonne

Dieter Goretzki

Akazienstr. 16, 63505 Langenselbold, Germany, Email: d.goretzki@t-online.de

Zusammenfassung

In der vorliegenden Arbeit werden die Ergebnisse spektroskopischer Untersuchungen der Lutetium II – Linie bei 6222 Å auf der Sonne vorgestellt. Diese Linie ist mit einer Äquivalentweite von < 1 mÅ sehr schwach. Trotzdem ist die Hyperfeinstruktur deutlich zu erkennen. Die Elementkonzentration von Lutetium auf der Sonne wird ermittelt.

Abstract

In this study, the results of spectroscopic investigations of lutetium II - line at 6222 Å on the sun. This line is very weak with an equivalent with of < 1 mÅ. Nevertheless, the hyperfine structure is clearly visible. The elemental concentration of lutetium on the sun is determined.

1. Einführung

Das Element Lutetium (Ordnungszahl 71, im deutschsprachigen Raum früher als Cassiopeium bezeichnet) ist neben Thulium eines der seltensten stabilen Elemente auf der Sonne. Interessanterweise ist es aber in der Erdkruste ca. 10mal häufiger vertreten als Silber, hat aber technisch keine Bedeutung erlangt.

In den bekannten Tabellen von Moore et al. (1966) sind auf der Sonne drei Linien des Lutetiums aufgeführt, die aber alle im UV-Bereich (< 3500 Å) liegen und für Amateure nicht erreichbar sind. Außerdem sind diese Linien durch „blends" gestört. Erst 1997 konnten D.J. Bord et al. [1] eine sehr schwache spektrale Signatur bei 6222 Å im Sonnenspektrum eindeutig dem Element Lutetium zuordnen. Diese Linie ist kaum gestört und durch die genaue Vermessung der Äquivalentbreite konnte die bis dahin bestehende Diskrepanz der Häufigkeiten von Lutetium auf der Sonne und in Meteoriten beseitigt werden.

Das Besondere an dieser sehr schwachen Linie ist die Tatsache, dass sie wegen der recht großen Hyperfeinstrukturaufspaltung aus zwei deutlich getrennten Teilen besteht.

2. Hyperfeinstruktur der Lu II Linie

Lutetium kommt auf der Erde als Isotope ^{175}Lu (Häufigkeit 97,41 %) und ^{176}Lu (2,59 %) vor. Während ^{175}Lu stabil ist, ist das Isotop ^{176}Lu schwach radioaktiv mit einer Halbwertzeit von ca. 10^{10} Jahren. Es kann deshalb zur Altersbe-

stimmung von sehr alten Gesteinen herangezogen werden. Beide Isotope haben eine ungerade Zahl an Protonen und/oder Neutronen, so dass der nicht ausgeglichene Kernspin eine Hyperfeinstrukturaufspaltung (Hfs) einiger Spektrallinien verursacht. Da das Isotop ^{176}Lu nur zu weniger als 3 % vertreten und die zu beobachtende Linie ohnehin sehr schwach ist, wurde bei den Untersuchungen dieses Isotop nicht weiter berücksichtigt.

Das Spektrum von Lutetium und die Hyperfeinstrukturaufspaltung einzelner Linie wurde schon sehr früh (1935) von H. Schüler und T. Schmidt vermessen [2], siehe Abb. 1.
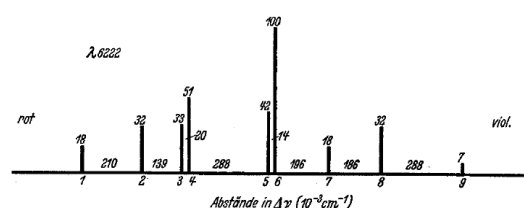

Abb. 1: Gemessenes Aufspaltungsmuster der Linie bei 6222 Å. Quelle Ref. 2.

Die Linie bei 6222 Å besteht aus insgesamt 9 einzelnen Komponenten. Das Aufspaltungsmuster kann theoretisch nach den folgenden Formeln berechnet werden, wobei der Kernspin für das Isotop ^{175}Lu I = 7/2 beträgt:

$$E_{hfs} = \frac{AK}{2} + B\frac{\frac{3}{4}K(K+1) - I(I+1)J(J+1)}{2I(2I-1)J(2J-1)}$$

$$K = F(F+1) - J(J+1) - I(I+1)$$

Der Übergang der Linie erfolgt zwischen den beiden Energieniveaus:

Unteres Niveau: 5d6s $^3D_2$ bei 12435,32 cm^{-1}

A = 64,38 mK

B = 45,8 mK

J = 2

Oberes Niveau: 6s6p $^3P_1$ bei 28503,16 cm^{-1}

A = 165,38 mK

B = -61,1 mK

J = 1

Die Konstanten A und B wurden [3] entnommen und mit diesen Angaben die in der Abb. 1 angegeben Energiedifferenzen berechnet. Wie die Tabelle 1 zeigt, ist die Übereinstimmung mit den Messungen gut.

Linie	Rechnung ΔE [cm^{-1}]	Messung ΔE [cm^{-1}]
1 - 2	0,208	0,210
2 - 3	0,140	0,139
3 - 4	0,019	0,020
4 - 5	0,287	0,288
5 - 6	0,017	0,014
6 - 7	0,191	0,196
7 - 8	0,190	0,186
8 - 9	0,287	0,288

Tab. 1: Vergleich zwischen Messung und Rechnung.

Die Hfs-Aufspaltung der Linie ist sehr groß und umfasst einen Bereich von ca. 0,5 Å.

3. Beobachtungspraxis

Die Beobachtungen wurden mit Hilfe des CT2000 [4] durchgeführt. Das Bild der Sonne ($\varnothing$ 16 mm) wurde mit einem 4"-SC (f/D = 10) auf einen Schirm projiziert. Der Eingang des LWL wurde hinter einem Loch mit Durchmesser 0,5 mm positioniert und das Licht der Sonnenmitte eingefangen. Die Belichtungszeit betrug 25 s. Nach der Aufnahmeserie wurden unmittelbar Flat- und Dark-Spektren erstellt. Die Reduktion des Spektrums erfolgte mit ESO-MIDAS® [5].

Die Spektren wurden in der 7. Ordnung des Blaze-Gitters gewonnen. Dazu war es erforderlich, den zu beobachtenden Spektralbereich durch einen Bandpassfilter einzugrenzen. Dieser wurde aus der Kombination eines Kurzpass- und eines Langpass-Interferenzfilters realisiert.

Bei vorangegangenen Testaufnahmen wurde festgestellt, dass ein 2x2-Binning des CCD deutlich bessere Ergebnisse hinsichtlich des Untergrundrauschens lieferte als das sonst von mir eingesetzte 1x1-Binning. Durch diese Maßnahme konnte außerdem die Belichtungszeit deutlich reduziert werden. Es wurde eine Serie von 10 Aufnahmen gewonnen, die bei der Reduktion gemittelt wurden.
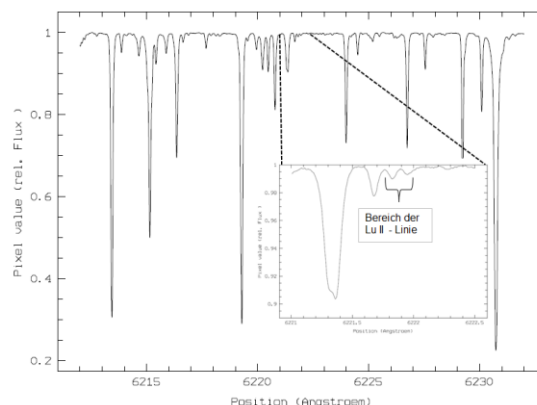

Abb. 2: Übersichtsspektrum um den Bereich der Lu II - Linie.

4. Auswertung

Wie das Übersichtsspektrum in Abb. 2 zeigt, ist die spektrale Signatur der Linie im Sonnenspektrum schon sehr schwach. Deshalb wurde dieser Bereich nach einer groben Normalisierung des Spektrums nochmals fein justiert. Obwohl es so aussieht, als ob es sich um zwei eigenständige Linien handelt, wird die spektrale Signatur nur durch einen Übergang hervorgerufen.

Zur Modellierung des Profils der Linie wurde jede einzelne der 9 Hfs-Komponenten durch Gauß-Profile approximiert und überlagert. Das Ergebnis zeigt die Abb. 3. Hier sind die einzelnen Übergänge der Hyperfeinstruktur mit eingezeichnet. Man erkennt deutlich, dass die „beiden" Linien nur durch die weit getrennten Hfs-Übergänge gebildet werden. Allerdings war es nicht einfach dieses Spektrum zu reproduzieren. Bei manchen Aufnahmeserien war die Struktur der Linie gar nicht zu erkennen. Ob das ggf. an der Luftunruhe lag, konnte nicht abschließend aufgeklärt werden. Auch brachte es keine Vorteile, mehr als 10 Spektren zu überlagern.

In der Abb. 4 ist als Vergleich das Ergebnis mit einem professionellen Spektrum (Labs & Neckel [6]) dargestellt.
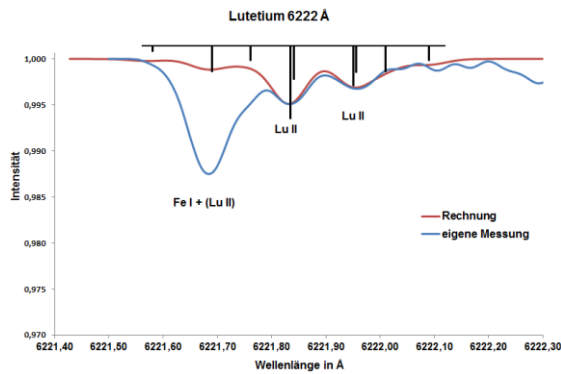
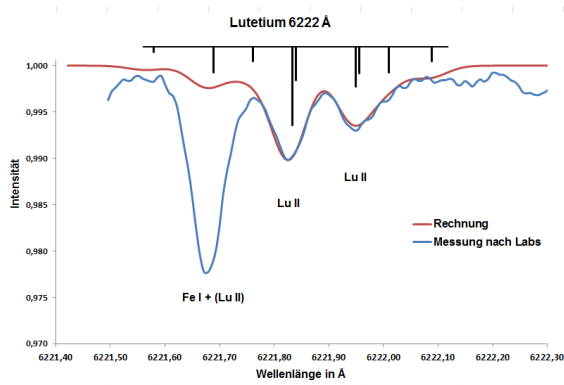**Abb. 3:** Struktur der Lu II – Linie im Vergleich zur Rechnung.

Abb. 4: Vergleich mit einem professionellen Spektrum von Labs & Neckel [6].

5. Bestimmung der Elementkonzentration

Die untersuchte Linie des Lutetiums ist sehr schwach. Deshalb wurde zur Auswertung nur das Spektrum von Labs & Neckel herangezogen. Bei schwachen Linien ist die Säulenkonzentration eines Elementes [Atome/m²] der Äquivalentbreite direkt proportional [7]. Die Formel dazu lautet:

$$A_\lambda = \frac{\pi \cdot e^2}{m_e \cdot c^2} \cdot \frac{\lambda^2 \cdot N \cdot H \cdot f}{4 \cdot \pi \cdot \varepsilon_0}$$

Darin bedeuten A_λ die Äquivalentbreite der Linie [m], λ die Wellenlänge der Linie [m], N H die Säulenhöhe [Atome/m²] und f die Oszillatorenstärke. Die weiteren Elementarkonstanten haben ihre übliche physikalische Bedeutung.

Die Linie besteht aus zwei Teilen. Deshalb wurde die Äquivalentbreite für beide Teile separat ermittelt.

Rote Linie: $3{,}33 \cdot 10^{-4}$ Å
Blaue Linie: $4{,}16 \cdot 10^{-4}$ Å
Summe: $7{,}49 \cdot 10^{-4}$ Å

Nun ist aber zu berücksichtigen, dass mit diesem Messwert nicht die vollständige Linie erfasst wird. Dies zeigt die Abb. 4 mit z.B. den Komponenten unter der Fe-Linie. Die Korrektur kann aus den relativen Anteilen der einzelnen Komponenten abgeschätzt werden, die bei der Bestimmung der Äquivalentbreite nicht berücksichtigt werden konnten. Die effektive Äquivalentbreite beträgt damit $\sim 1 \cdot 10^{-3}$ Å.

Die Rechnung ergibt mit diesem Wert eine Säulenhöhe von $8{,}6 \cdot 10^{14}$ Atome/m², wobei mit einem f von 0,034 (siehe dazu NIST Atomic Spectra Database [8]) gerechnet wurde. Allerdings wurde hier nur eine Linie ausgewertet. Um alle Atome des einfach ionisierten Lutetiums die „irgendwie" angeregt sind zu erfassen, hilft die bekannte Boltzmann-Formel:

$$\frac{N_{i,m}}{N_i} = \frac{g_{i,m}}{u_i(T)} \exp\left(-\frac{\chi_{i,m}}{kT}\right)$$

Für die Bedingungen der Photosphäre (Temperatur ~5800 K) erhält man eine Korrektur von 0,1. Das bedeutet, dass etwa 10mal mehr Atome einfach ionisiert sind als durch die Bestimmung nur einer Linie ermittelt wurden. Die Säulendichte ergibt sich somit zu $8{,}6 \cdot 10^{15}$ Atome/m².

Des Weiteren sind die Atome zu berücksichtigen, die nicht ionisiert oder doppelt ionisiert sind. Hier hilft die Saha-Gleichung. Eine überschlägige Rechnung zeigt aber, dass nur etwa 1 % aller Atome nicht ionisiert ist. Zum Vergleich liegt dieser Wert für Natrium mit einer etwas geringeren Ionisationsenergie bei ca. 0,3 %. Diese Korrektur kann deshalb vernachlässigt werden. Zweifach ionisiertes Lutetium ist unter den Bedingungen der Photosphäre auf der Sonne nicht zu erwarten (Ionisationsenergie ca. 15 eV).

Somit beträgt die Säulendichte wie angegeben $8{,}6 \cdot 10^{15}$ Atome/m². Um diesen Wert mit den Angaben in der Literatur zu vergleichen, wird er auf Wasserstoff bezogen und auf 10^{12} normiert. Die Säulendichte für Wasserstoff wird auf der Sonne mit ca. $6{,}6 \cdot 10^{27}$ Atome/m² angegeben.

Damit erhält man:
[Lu] = log($8{,}6 \cdot 10^{15}$) - log($6{,}6 \cdot 10^{27}$) + log(10^{12})
[Lu] = 15,93 - 27,82 + 12 = 0,11

Dieser Wert passt gut mit den Angaben aus dem Review Ref. 9 überein:
Sonne: 0,10 ± 0,09
Meteorit: 0,09 ± 0,02

6. Fehlerbetrachtung

Schwerpunkt dieser Arbeit sind phänomenologische Untersuchungen zur Hfs-Aufspaltung. Die Übereinstimmung der berechneten Hfs-Aufspaltungen mit den Messungen von Schüler und Schmidt ist gut. Die Linien können mit Hilfe dieser Rechnungen reproduziert werden. Um die eigenen Messungen zu reproduzieren, musste eine Verbreiterung der Einzellinien mit einer FWHM vom 0,0749 Å als Superposition von Gaußprofilen durchgeführt werden. In diesem Spektralbereich entspricht dies einer Auflösung des Spektrografen von
$R = 6222 / 0,0749 = 83.000$.

Die schwächere Auflösung gegenüber einem professionellen Gerät wird in der Abb. 4 deutlich. Während bei mir die maximale Linieneinsenkung nur ca. 0,5 % vom Kontinuum beträgt, werden bei Labs und Neckel 1 % erreicht.

Nach der Rechnung liegt der Linienschwerpunkt der Lutetium-Linie (für Luft) bei 6221,891 Å. Dies entspricht der Angabe in der VALD-Datenbank: 6221,890 Å [10].

Für die Elementkonzentration gelten die üblichen Unsicherheiten, die im Wesentlichen die Bestimmung der Äquivalentbreite betreffen (< 10 %). Die ermittelte Elementkonzentration ist vergleichbar mit dem Literaturwert, obwohl nur eine Linie ausgewertet wurde.

Literatur

[1] D.J. Bord, C.R. Cowley and D. Mirijanian, Sol. Phys. 178 (1998) 22
[2] H. Schüler und T. Schmidt, Z. Physik, 95 (1935) 265
[3] C. Sneden et al., ApJ, 591 (2003) 936
[4] D. Goretzki, Spektrum 39 (2010) 4
http://spektroskopie.fg-vds.de/pdf/Spektrum39.pdf
[5] ESO-MIDAS,
http://www.eso.org/sci/software/esomidas/doc/index.html
[6] http://www.hs.uni-hamburg.de/DE/Oef/Inf/Einbl/Sospec/sonnspec.html
[7] H. Scheffler und H. Elsässer, Physik der Sterne und der Sonne, BI Wissenschaftsverlag
[8] A. Kramida, Y. Ralchenko, J. Reader and NIST ASD Team (2015). NIST Atomic Spectra Database, Online: http://physics.nist.gov/asd
[9] M. Asplund et al., Annual Rev. Astro. & Astrophys. 47 (2009) 481 and arXiv:0909.0948v1
[10] VALD Vienna Atomic Line Database, http://vald.astro.univie.ac.at/~vald3/php/vald.php?newsitem=0

Dieter Goretzki beschäftigt sich seit mehr als 15 Jahren mit der Spektroskopie. Angefangen hatte alles mit einem Objektiv-Prisma und SW-Film. Später gilt sein Interesse besonders der Photosphäre der Sonne, die er mit einem selbst gebauten fasergekoppelten Spektrografen von 2 m Fokalweite untersucht.

Nur für Mitglieder der Fachgruppe Spektroskopie in der
Vereinigung der Sternfreunde e.V.

For members of the Section Spectroscopy
of the Society of German Amateur Astronomers only.

Besuchen Sie / Visit

spektroskopie.fg-vds.de

**und werden Sie Mitglied. Einfach per Mail an den Sprecher
der Fachgruppe.**

**and become a member by sending an e-mail to the spokes-
man of the section.**